Photochemical and photophysical dynamics of the aqueous ferrate(VI) ion

Cali Antolini,[1] Charles D. Spellman, Jr.,[2] Christopher J. Otolski,[3] Gilles Doumy,[3] Anne Marie March,[3] Donald A. Walko,[4] Cunming Liu,[4] Xiaoyi Zhang,[4] Benjamin T. Young,[5] Joseph E. Goodwill,[2] and Dugan Hayes*[1]

[1]Department of Chemistry, University of Rhode Island, 45 Upper College Road, Kingston, RI 02881, USA

[2]Department of Civil and Environmental Engineering, University of Rhode Island, 45 Upper College Road, Kingston, RI 02881, USA

[3]Chemical Sciences and Engineering Division, Argonne National Laboratory, 9700 S. Cass Avenue, Argonne, Illinois 60439, USA

[4]X-ray Science Division, Argonne National Laboratory, 9700 S. Cass Avenue, Argonne, Illinois 60439, USA

[5]Department of Physical Sciences, Rhode Island College, 600 Mt Pleasant Ave., Providence, RI 02908, USA

ABSTRACT: Ferrate(VI) has the potential to play a key role in future water supplies. Its salts have been suggested as "green" alternatives to current advanced oxidation and disinfection methods in water treatment, especially when combined with ultraviolet light to stimulate generation of highly oxidizing Fe(V) and Fe(IV) species. However, the nature of these intermediates, the mechanisms by which they form, and their roles in downstream oxidation reactions remain unclear. Here we use a combination of optical and X-ray transient absorption spectroscopies to study the formation, interconversion, and relaxation of several excited-state and metastable high-valent iron species following excitation of aqueous potassium ferrate(VI) by ultraviolet and visible light. Branching from the initially populated ligand-to-metal charge transfer state into independent photophysical and photochemical pathways occurs within tens of picoseconds, with the quantum yield for generation of reactive Fe(V) species determined by relative rates of the competing intersystem crossing and reverse electron transfer processes. Relaxation of the metal-centered states then occurs within 4 ns, while the formation of metastable Fe(V) species occurs in several steps with time constants of 250 picoseconds and 300 nanoseconds. Results here improve the mechanistic understanding of the formation and fate of Fe(V) and Fe(IV), which will accelerate the development of novel advanced oxidation processes for water treatment applications.

INTRODUCTION

Ensuring adequate water supplies is one of the grand challenges of the 21st century,[1] and the tetrahedral $[FeO_4]^{2-}$ ion, known as ferrate(VI), may play a key role in this area. Salts of ferrate(VI) are the only known shelf-stable hexavalent iron compounds, making them incredibly powerful and versatile stores of oxidizing potential.[2] For example, both potassium and barium ferrate(VI) have been employed as selective oxidizing agents in organic syntheses,[3–8] and potassium ferrate(VI) has been used to transform trace organic contaminants (TOCs) in water treatment applications.[9–11] Crucially for practical large-scale use, these durable, non-toxic salts are also comprised entirely of earth-abundant elements and may be prepared in bulk quantities through straightforward chemical[12,13] and electrochemical syntheses.[14–16]

Water supplies are threatened by TOCs from urban and agricultural run-off, industrial activity, and wastewater treatment plants,[10,17] and mitigation of these TOCs is projected to require a high level of effort and focus in the near term.[1] Treatment of TOCs has been accomplished with chlorine-based oxidants (*e.g.*, hypochorite, chlorine dioxide) with some success; however, this approach can lead to the formation of halogenated disinfection byproducts, including trihalomethanes and haloacetic acids.[17–20] Also, some recalcitrant TOCs are not amenable to such oxidizing agents. Advanced oxidation processes (AOPs) – processes involving the addition of multiple reagents to form highly reactive, transitory species – have proven effective, typically involving ozone, hydrogen peroxide and/or ultraviolet (UV) light.[19] Tradeoffs with existing AOPs include the need for on-site generation of inputs and byproduct formation.[21]

Ferrate(VI) has a pH-dependent reduction potential that is higher than that of ozone and chlorine dioxide under acidic conditions,[8,22] and its direct byproducts are non-toxic, insoluble Fe(III) oxides that may support downstream coagulation and filtration processes in water treatment systems.[23,24] Improved transformation of TOCs

can be achieved through "activation" of ferrate(VI) – the addition of aqueous phase reductants,[25–27] acids,[28,29] carbonaceous materials,[30,31] or UV light.[18,32,33] The improvement in effectiveness can be attributed to the formation of Fe(V) (perferryl) and Fe(IV) (ferryl) intermediates,[25,26,34] which, like the hydroxyl radicals formed in other AOPs, are several orders of magnitude more reactive than the parent Fe(VI) ion toward target compounds.[9,35,36] Since the Fe(V) species are known to have the higher reduction potentials, most proposed mechanisms for either direct oxidation of TOCs or generation of intermediary oxidizing species (*e.g.*, hydroxyl radicals) with activated ferrate invoke a pentavalent iron intermediate,[9,18,33–35] though recent studies have suggested that Fe(IV) species likely play a significant role as well.[32]

The ephemeralness of these intermediates and the unavoidably complex web of interconnected radical pathways in these reactions, however, present a substantial challenge for unambiguously identifying and tracking individual species using conventional spectroscopic techniques and analyses. Prior attempts to separate the roles of contemporaneous radicals within the activated ferrate system have included (1) adding aqueous phase reductants in excess to quench any Fe(V/IV); (2) using probe compounds such as *tert*-butanol, ethanol, and dimethyl sulfoxide to quench specific radicals, (3) studying ferrate reactions in anaerobic conditions, and (4) assessing radical-adducts *via* electron paramagnetic resonance.[25,37,38]. These approaches have helped elucidate the roles of such intermediates, but direct observation of ferryl and/or perferryl intermediates toward the development of a full mechanistic understanding of this water treatment approach has remained elusive.

The optical absorption spectra of aqueous ferrate(V) (that is, Fe(V)-containing $[FeO_4]^{3-}$) buffered at several pH values have been previously measured by Bielski, Rush, Sharma, and coworkers using pulse radiolysis.[35,36,39–42] This technique, in which short electron pulses are used to generate unstable reduced and/or oxidized species, was also used to monitor decay and oxidation kinetics of ferrate(V) intermediates in real time with microsecond to millisecond resolution. Similarly, Roth and coworkers used a stopped-flow pH-jump method to measure the kinetics of water oxidation by ferrate(VI) in acidic solution by monitoring the optical absorption spectrum over time,[43] while Novak *et al.* used ^{57}Fe Mössbauer spectroscopy to quantify the Fe(III) – Fe(VI) content of freeze-quenched aqueous and ethanolic solutions of ferrates (IV), (V), and (VI).[44] Other short-lived Fe(V) and Fe(IV) complexes generated photochemically from lower-valent precursors have been studied by optical and infrared transient absorption spectroscopies,[45–47] while the steady-state spectroscopic properties (EPR, vibrational, optical, X-ray, Mössbauer, etc.) of isolable Fe(IV) – Fe(VI) compounds have been exhaustively documented due to the prevalence of high-valent iron centers in metalloenzymes.[48–67] Surprisingly, however, direct spectroscopic measurements of the excited state dynamics of ferrate(VI) have not been reported.

Due to the high density of electronic states in ferrate(VI), several competing assignments of the optical transitions have been presented over the past six decades. The d^2 tetrahedral/d^8 octahedral Tanabe-Sugano diagram provides a framework for ordering the ligand field (or metal-centered, MC) states relative to the $^3A_2$ ground state,[68] showing that the lowest energy transitions for a realistic ligand field splitting are the spin-forbidden transitions to the ^1E and $^1A_1$ states. The earliest published absorption spectra of aqueous ferrate(VI) did not extend sufficiently into the near-infrared to find the bands corresponding to these transitions,[69] but Orgel assigned the bands at 790 nm (12700 cm^{-1}) and 510 nm (19600 cm^{-1}) to the $^3A_2 \rightarrow {}^3T_2$ and $^3A_2 \rightarrow {}^3T_1$ transitions, respectively.[70] Itoh first identified a weak band at 1.1 μm (9100 cm^{-1}) and assigned it to the $^3A_2 \rightarrow {}^1E$ transition in 1976,[71] and Güdel and coworkers reported an even lower energy band at 1.6 μm (6200 cm^{-1}) in both the absorption and emission spectra of cryogenic ferrate(VI)-doped K_2CrO_4 crystals in the early 1990s, assigning it to the $^3A_2 \rightarrow {}^1E$ transition and revising the assignment of the 1.1 μm band to the $^3A_2 \rightarrow {}^1A_1$ transition.[72,73]

Restricted active space self-consistent field calculations reported by Al-Abdalla *et al.* in 1998 show that the d^2 ligand field theory model is inadequate in capturing the complexity of the electronic structure, as the strong covalency in ferrate(VI) results in substantial mixing of the higher energy *d-d* transitions and ligand-to-metal charge transfer (LMCT) states.[74] Nevertheless, the authors assigned the broad visible absorption band spanning from 450 to 600 nm to transitions to two clusters of ^{3}MC states (both $^3T_1$) with some ^{1}MC and charge transfer character

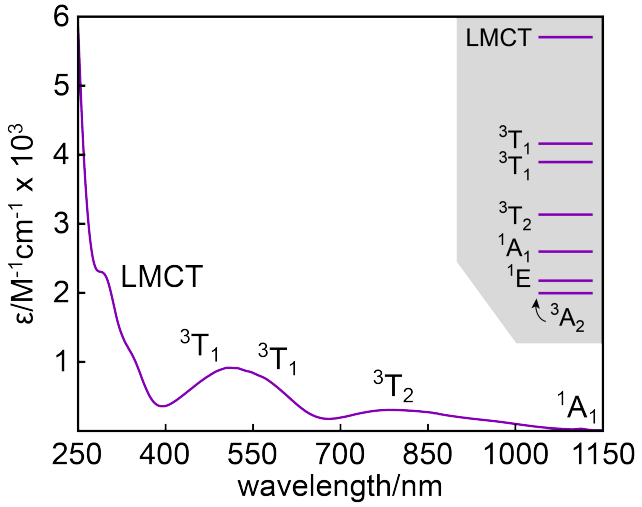

Figure 1. Steady-state UV-visible absorption spectrum of ferrate(VI). The absorption in the UV corresponds to several LMCT transitions from the $^3A_2$ ground state. Two $^3T_1$ ligand field bands and one $^3T_2$ band are apparent in the visible, while the weak spin-forbidden $^1A_1$ band appears in the near-infrared. (Inset) Relative energy spacings of the ground and excited states of ferrate(VI).

and absorption in the UV to a cluster of ^{5}LMCT states. The steady-state absorption spectrum of potassium fer-

rate(VI) and the average relative energy spacings of its excited states aggregated from the references discussed above are presented in Fig. 1.

The only excited state absorption (ESA) spectrum of ferrate(VI) to date was presented by Brunold *et al.* in 1996.[75] The authors measured the spectrum of a ferrate(VI)-doped K_2SO_4 crystal at room temperature while pumping the visible absorption band with a chopped cw argon ion laser, finding a strong band at 750 nm (13300 cm^{-1}) that they assigned to the $^1E \rightarrow {}^1T_2$ transition. The same group had previously found the lifetime of the 1.6 µm photoluminescence to be ~0.6 ms at 0 °C.[73] Importantly, they also reported a strong temperature dependence of the quantum yield of this emission band, suggesting that nonradiative internal conversion (IC) to the ground state from the ^{3}MC states begins to outcompete intersystem crossing (ISC) to the ^{1}MC states at elevated temperatures.

In this work, we use a combination of multiwavelength optical transient absorption (OTA) and X-ray transient absorption (XTA) spectroscopies to disentangle the competing photophysical and photochemical pathways in ferrate(VI) following UV excitation. OTA gives us a picture of these dynamics with ultrafast resolution, while XTA provides an element-specific probe of the oxidation state of iron. By performing these experiments using visible, near-infrared (NIR), and UV excitation, we first investigate the dynamics of the MC states and then use these insights to inform our analysis of the dynamics following charge transfer. Our results indicate that within the first 50 ps, relaxation from the initially populated ^{3}LMCT Fe(V)* state diverges between 1) reverse electron transfer to yield Fe(VI)* ^{3}MC states that ultimately relax to the ground state, and 2) ISC to a ^{5}LMCT Fe(V)* state that ultimately abstracts a hydrogen atom from the solvent to give the metastable $[FeO_3(OH)]^{2-}$ species. Because only the second pathway produces the perferryl species responsible for oxidation of TOCs, the branching ratio gives us the quantum yield for UV activation of ferrate(VI). In addition to the implications for water treatment applications, these results provide the first time-resolved picture of the excited state dynamics of ferrate(VI), showing how light stimulates the incredible oxidizing potential of this uniquely high-valent iron species.

RESULTS AND DISCUSSION

X-ray transient absorption

General procedures. Steady-state and transient X-ray absorption spectra were acquired at beamline 7-ID-D at the Advanced Photon Source (APS) at Argonne National Laboratory with the storage ring operating in 24 bunch mode. The ground state iron K-edge X-ray absorption near edge structure (XANES) spectrum of aqueous potassium ferrate(VI) buffered at pH 8.6 is shown in Fig. 2A. Because ferrate(VI) is rapidly photoreduced by the intense X-ray beam at an insertion device beamline and the sample thus could not be recirculated, only a narrow energy range was measured for the XANES scans. However, the pre-edge peak at 7.115 keV provides a clear probe of the occupation of the iron 3*d* orbitals, while the energy of the edge reports on the oxidation state of the iron center. The pre-edge observed here is remarkably intense due to the tetrahedral geometry of the complex,[76] which imparts substantial dipole character to the nominally quadrupole-allowed 1*s* → 3*d* transition through mixing of the 3*d* and 4*p* orbitals.

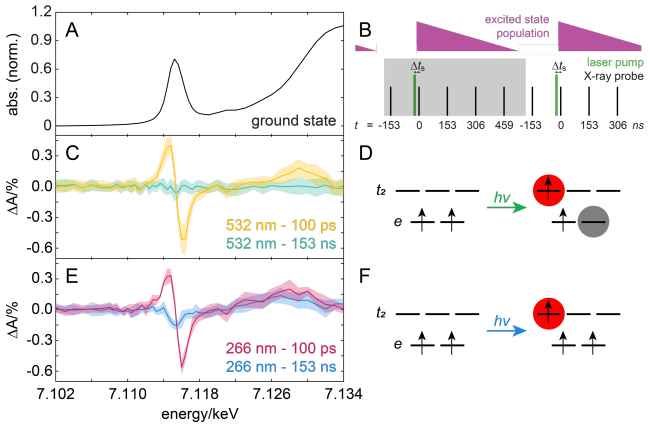

Figure 2. Steady-state and transient iron K-edge spectra of aqueous potassium ferrate(VI). (A) Ground state XANES spectrum. (B) Pulse sequence used for XTA measurements. The laser "pump" (green) is synchronized with the X-ray "probe" (black) at one-fifth the repetition rate, giving the measurement window indicated by the gray box. The sample flow rate is tuned such that the optically excited sample (plum) leaves the beam overlap position by the arrival of the fifth pulse. (C) XTA difference spectra following excitation at 532 nm at Δt = 100 ps (yellow) and 153 ns (teal). (D) Schematic of the excitation to the ^{3}MC state, highlighting the origin of the ESA (gray circle) and GSB (red circle) peaks. (E) XTA difference spectra following excitation at 266 nm at Δt = 100 ps (red) and 153 ns (blue). (F) Schematic of the excitation to the LMCT state, highlighting the origin of the GSB peak (red circle).

XTA measurements were performed with the optical laser operating at a repetition rate equal to one fifth that of the storage ring (1.30 and 6.52 MHz, respectively) and the sample jet delivering a fresh sample at the laser/X-ray overlap position at approximately the same rate as the laser.[77] In this mode, we can measure three X-ray probe pulses for each laser shot, as depicted schematically in Fig. 2B: 1) a ground state reference before the arrival of the laser pulse (*i.e.*, negative pump-probe delay time, $\Delta t <$ 0); 2) a short Δt (Δt_s) with ~80 ps temporal resolution; and 3) a long $\Delta t = \Delta t_s$ + 153 ns, which is the time interval between sequential X-ray pulses. Although the next two pulses roughly correspond to values of Δt at additional 153 ns intervals, a significant amount of the photoexcited sample has already escaped the X-ray beam position at these times, and thus any analysis of the data acquired with these probe pulses must account for this effect.

Visible excitation. Difference spectra ("laser on" minus "laser off") following excitation of the *d*-*d* band at 532 nm are shown in Fig. 2C at Δt = 100 ps (yellow) and 153 ns

(teal); the solid lines are the average of several (typically nine) measurements and the shaded regions indicate the standard deviation of these measurements. The spectrum at 100 ps shows a prominent excited state absorption (ESA) peak on the red side of the pre-edge with a maximum at 7.1145 keV and a ground state bleach (GSB) peak on the blue side with a minimum at 7.1160 keV. Within the tetrahedral crystal field picture shown in Fig. 2D, the optical transition corresponds to the creation of a hole in the *e* orbitals and the loss of a hole in the t_2 orbitals, resulting in the derivative-like XTA feature seen here. We note that for the ground $^3A_2$ state, only the $1s \rightarrow t_2$ transitions are dipole allowed, accounting for the single pre-edge peak observed here.[78] In the $^3T_2$ excited state, however, the $1s \rightarrow t2$ and the $1s \rightarrow e$ transitions are dipole allowed. Accordingly, what we observe in our difference spectrum, to a first approximation, is the loss of some of the $1s \rightarrow t_2$ intensity (GSB) and the growth of the $1s \rightarrow e$ intensity (ESA). A broad positive band at 7.1290 keV is also observed, likely arising from the $1s \rightarrow 4p$ transitions. Kinetic traces measured at the ESA and GSB peaks are shown in Fig. 3A-B. Both features decay monoexponentially with an average time constant of 3.8 ns (Fig. S2A-B) with no evidence of any long-lived species (these time constants are collected in Table 1, and all fit parameters are given in Table S1). Thus, we may conclude that the lifetime of the ^{3}MC state is 3.8 ns under these conditions.

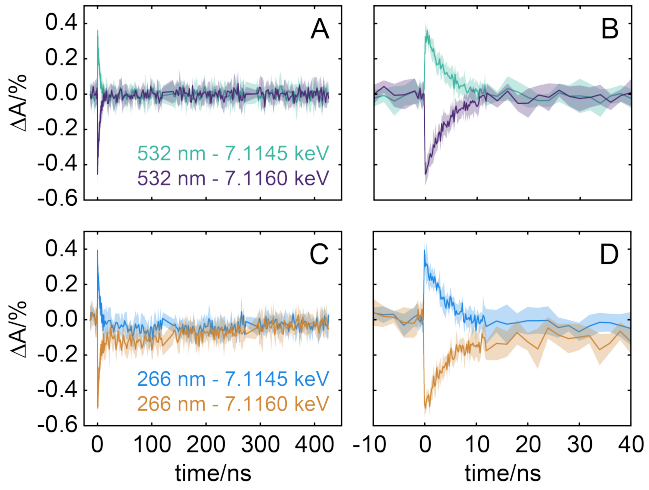

Figure 3. XTA kinetic traces. (A) Full XTA kinetic traces measured at 7.1145 keV (teal) and 7.1160 keV (purple) following excitation at 532 nm. (B) Early time window of the data in panel (A). (C) Full kinetic traces measured at 7.1145 keV (blue) and 7.1160 keV (orange) following excitation at 266 nm. (D) Early time window of the data in panel (C).

Ultraviolet excitation. Difference spectra following excitation of the LMCT band at 266 nm are shown in Fig. 2E at the same values of Δt (red and blue, respectively). The 100 ps spectrum closely resembles the ^{3}MC spectrum in Fig. 2C, but the amplitude of the ESA peak (7.1145 keV) relative to the GSB peak (7.1160 keV) is somewhat diminished and the broad positive band at the edge is even broader and centered at a slightly lower energy (7.1287 keV). Within 153 ns, the pre-edge ESA and GSB features associated with the ^{3}MC state have disappeared entirely, leaving only a GSB peak positioned at the center of the pre-edge at 7.1154 keV. In addition, the energy of the broad positive band has shifted even lower to 7.1273 keV. The kinetic traces shown in Fig. 3C-D are dominated by the same 3.8 ns decay observed following excitation of the *d-d* band, though additional slower components are also observed with time constants of 50 and 300 ns (Fig. S2C-F), with the former only appearing in the ESA. Importantly, the 300 ns time constant is comparable to the sample refreshment period (see SI for details), and thus it is not clear from these data alone if it arises at all from genuine excited state dynamics. Similarly, the 50 ns time constant should be taken as a qualitative estimate, as it is still within an order of magnitude of the refreshment period.

Table 1. Time constants obtained from XTA kinetic fits with 95% confidence intervals.

Pump (nm)	**266**		**532**	
Probe (keV)	7.1145	7.1160	7.1145	7.1160
τ_1 **(ns)**	3.7 ± 0.7	3.2 ± 0.4	3.6 ± 0.3	4.0 ± 0.3
τ_2 **(ns)**	50 ± 40	x	x	x
τ_3 **(ns)**	380*	380 ± 70	x	x

*Time constant was fixed for this fit. An entry of 'x' means no component was observed.

These spectra clearly reveal that the initially populated ^{3}LMCT state relaxes on the picosecond timescale principally into the ^{3}MC manifold, from which it returns to the ground state with a lifetime of 3.8 ns. This accounts for the striking similarity between the difference spectra and the kinetic traces at early Δt. Beyond 10 ns, however, the difference spectrum is consistent with Fe(V): occupation of the t_2 orbitals (Fig. 2F) gives rise to GSB but no ESA in the pre-edge, and an oxidative edge shift is apparent at 7.127 keV. Both the loss of pre-edge intensity and edge shift are in excellent agreement with the difference observed between the steady-state iron K-edge spectra of the penta- and hexavalent variants of high-valent iron model complexes.[53,66] We may thus assign these features to the ^{5}LMCT state and conclude that ISC is the minor relaxation pathway from the ^{3}LMCT state. Assuming the magnitudes of the GSB features of the transient species are approximately equal, we may perform a simple linear combination analysis of the 266 nm/100 ps difference spectrum using the 532 nm/100 ps and 266 nm/153 ns difference spectra as Fe(VI) and Fe(V) standards, respectively (see SI and Fig. S3 for details). From this, we find that ~90% of the ^{3}LMCT state relaxes *via* the ^{3}MC manifold and only ~10% undergoes ISC to give the long-lived perferryl species that are active toward oxidation of organic contaminants in water treatment applications.

To monitor the long-time behavior of the difference spectrum, XTA measurements with UV excitation were also performed using a 3.0 kHz excitation repetition rate

and a ~100 μs sample refreshment period at beamline 11-ID-D at the APS. Here, the delay window was limited to ~20 μs not by the sample flow rate but instead by the X-ray chopper used to limit the X-ray flux incident on the sample. The difference spectrum at 153 ns shown in Fig. 4 (blue) agrees well with that shown in Fig. 2E, and it is also qualitatively indistinguishable from the spectrum averaged between 153 ns and 18 μs on top of which it is plotted (purple). This demonstrates that the population and/or spectrum of the Fe(V) species does not change significantly between 100 ps and 10 μs, which is consistent with the few ms lifetimes observed in pulse radiolysis work.[40] Accordingly, the component of the 300 ns time constant observed in the high repetition rate XTA kinetic traces that originates from metastable and/or excited state dynamics is likely to be small.

The excellent signal-to-noise in the time-averaged spectrum in Fig. 4 also confirms the reproducibility of the small ESA shoulder at 7.113 keV seen in the 266 nm/100 ps spectrum but not in the 532 nm/100 ps spectrum in Fig. 2. Because this feature is not observed at 153 ns, we may associate it with the 50 ns time constant obtained from the fit of the non-monotonic kinetic trace of the ESA peak (Fig. S2E-F). The assignment of this time constant is discussed later.

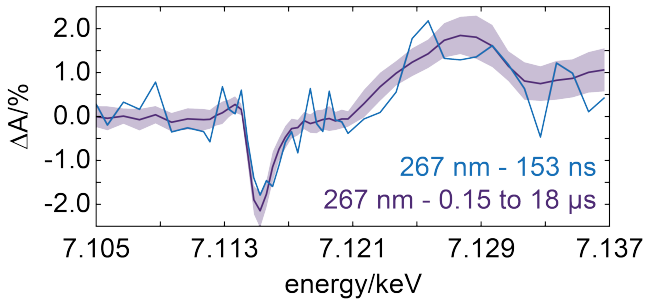

Figure 4. Long-time XTA difference spectra. Spectra measured following excitation at 267 nm using a 3.0 kHz excitation repetition rate at Δt = 153 ps (blue) and averaged over all X-ray probe pulses between 0.15 and 18 μs (purple).

Optical transient absorption

Visible excitation. While XTA provides an excellent probe of the dynamics of photoexcited ferrate(VI), the duration of the X-ray pulses at the APS limits the achievable temporal resolution to ~80 ps. To gain further insight, we complemented these studies with OTA measurements at both the fs/ps and ns/μs timescales. All OTA measurements were performed at kHz repetition rates using a recirculating sample pumped through a 0.5 mm pathlength quartz flow cell cuvette with a ~100 μs sample refreshment rate (see SI for more details).

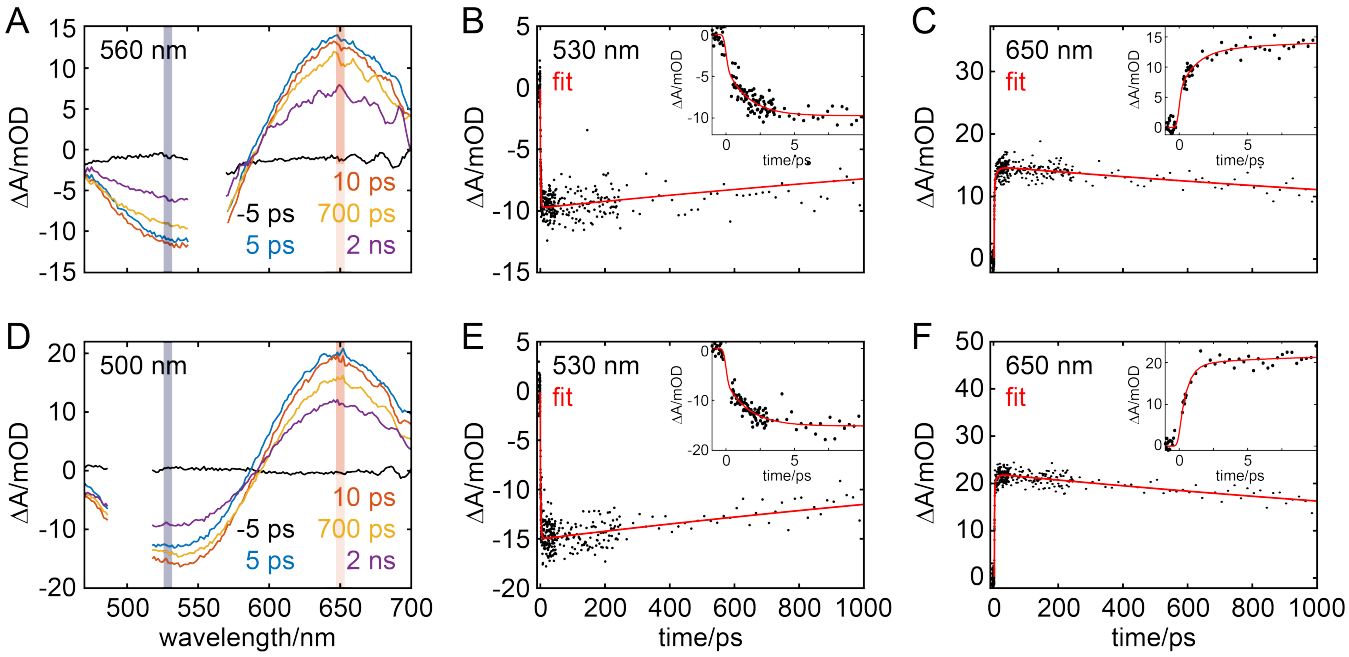

Figure 5. Ultrafast OTA spectra and kinetics with visible excitation. (A) OTA spectra plotted at several values of Δt following excitation at 560 nm, showing a GSB peak centered at 530 nm and an ESA peak centered at 650 nm. (B) Kinetic trace of the GSB averaged over the spectral window centered at 530 nm indicated in panel (A) by the gray vertical bar. The data points (black dots) were fit (red curve) to the sum of two exponential terms convolved with a Gaussian IRF after excluding the data points within 240 fs of the maximum of the strong coherent artifact. The inset shows the rise of the trace at Δt < 10 ps. (C) Kinetic trace of the ESA averaged over the spectral window centered at 650 nm indicated in panel (A) by the salmon vertical bar fit using the same function with an additional exponential term. (D) – (F) The same data and fits measured following excitation at 500 nm.

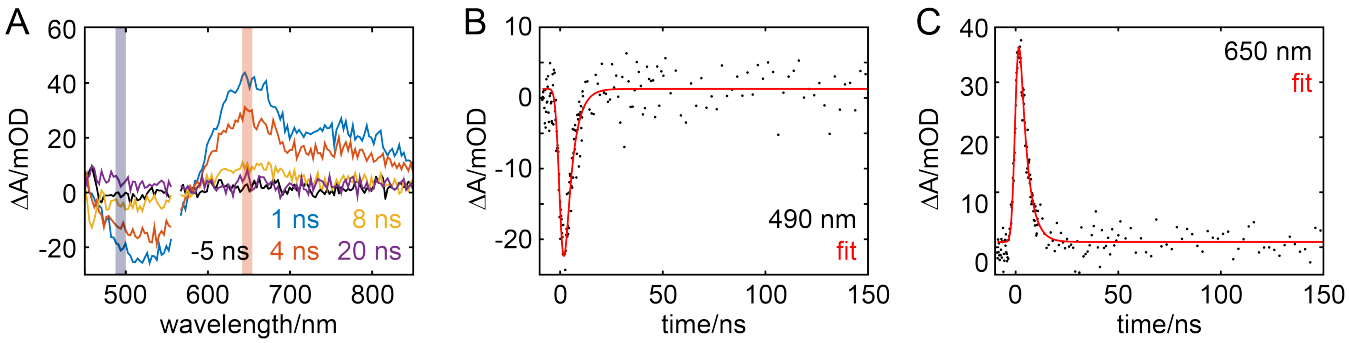

Figure 6. Nanosecond OTA spectra and kinetics with visible excitation. (A) OTA spectra plotted at several values of Δt following excitation at 560 nm, showing a GSB peak centered at 520 nm and ESA peaks centered at 650 and 775 nm. (B) Kinetic trace of the GSB averaged over the spectral window centered at 490 nm indicated in panel (A) by the gray vertical bar. The data points (black dots) were fit (red curve) to a single exponential term convolved with a Gaussian IRF. (C) Kinetic trace of the ESA averaged over the spectral window centered at 650 nm indicated in panel (A) by the salmon vertical bar fit using the same function.

Broadband ultrafast OTA spectra and kinetics following visible excitation are shown in Fig. 5. The sample was pumped at both 560 nm (panels (A)-(C)) and 500 nm (panels (D)-(F)), the wavelengths corresponding to the centers of the two $^3A_2 \rightarrow {}^3T_1$ *d-d* bands. For all $\Delta t > 0$, the difference spectra for both pump wavelengths exhibit GSB and ESA peaks centered at 530 nm and 650 nm, respectively. The fits of the ESA kinetic traces show three exponential components: two short rises with average time constants of 900 fs and 9 ps and a slow decay with a time constant of 3.4 ns that is consistent with the 3.8 ns ground state recovery time obtained from the XTA measurements (these time constants are collected in Table 2, and all fit parameters are given in Table S2). Importantly, a single short rise component cannot reproduce the kinetics at both very short (< 3 ps) and intermediate (3-20 ps) times. The fits of the GSB kinetic traces, however, show only the shorter rise and the slow decay, with average time constants of 1.7 ps and 3.7 ns, respectively. Although the states in the 500 nm band must relax through those in the 560 nm band, no statistically significant difference is observed between the kinetics measured for the two pump wavelengths in either the GSB or ESA, indicating that this relaxation is faster than the 300 fs resolution of the measurement determined from the width of the coherent artifact (see Fig. S4).

Because our fs OTA instrument is limited to $\Delta t < 2$ ns, the ~4 ns time constant obtained from the fits shown in Fig. 5 is only approximate, and we also cannot conclusively rule out the possibility of a residual long-lived signal. Accordingly, we performed ns OTA using 560 nm excitation to confirm what we observed in the XTA measurements. The OTA spectra in Fig. 6A are consistent with the fs-resolved spectra in Fig. 5A, showing distinct GSB and ESA peaks centered at 520 nm and 650 nm, respectively, that disappear nearly entirely within 10 ns. The broader white light continuum probe used in the ns OTA measurements also reveals an additional ESA peak

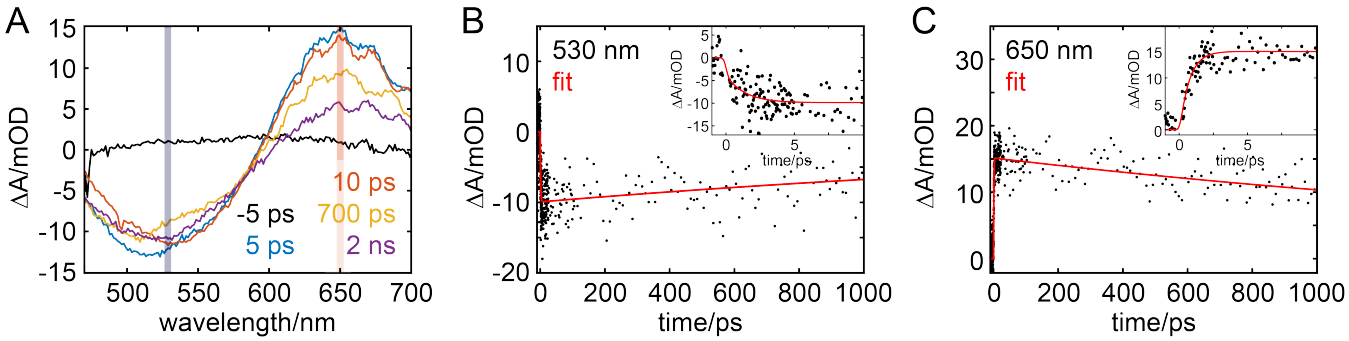

Figure 7. Ultrafast OTA spectra and kinetics with NIR excitation. (A) OTA spectra plotted at several values of Δt following excitation at 800 nm, showing a GSB peak centered at 530 nm and an ESA peak centered at 650 nm. (B) Kinetic trace of the GSB averaged over the spectral window centered at 530 nm indicated in panel (A) by the gray vertical bar. The data points (black dots) were fit (red curve) to the sum of two exponential terms convolved with a Gaussian IRF after excluding the data points within 240 fs of the maximum of the strong coherent artifact. The inset shows the rise of the trace at $\Delta t < 10$ ps. (C) Kinetic trace of the ESA averaged over the spectral window centered at 650 nm indicated in panel (A) by the salmon vertical bar fit using the same function.

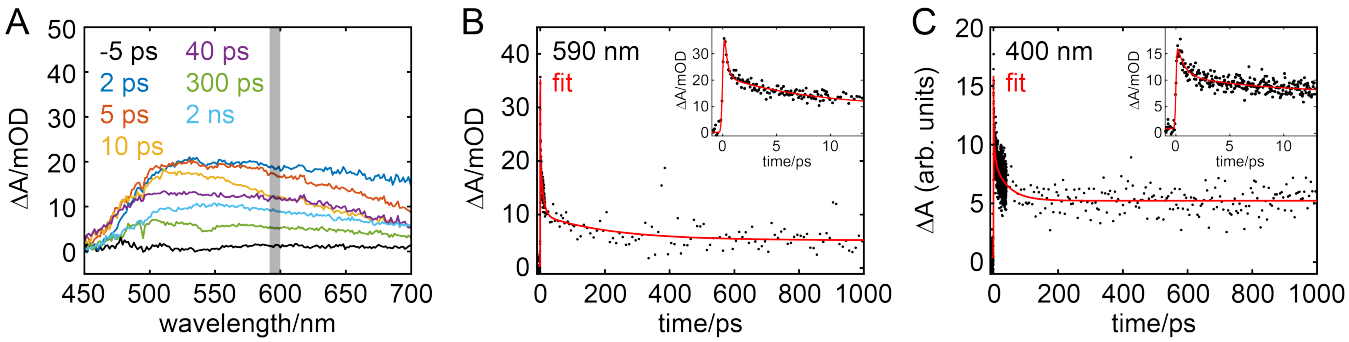

Figure 8. Ultrafast OTA spectra and kinetics with UV excitation. (A) OTA spectra plotted at several values of Δt following excitation at 267 nm, showing a featureless ESA band spanning the spectral window of the white light continuum probe. (B) Kinetic trace of the ESA averaged over the spectral window centered at 590 nm indicated in panel (A) by the gray vertical bar. The data points (black dots) are fit (red curve) to the sum of three exponential terms and a step function, all convolved with a Gaussian IRF. The inset shows the rise of the trace at Δt < 13 ps. (C) OTA kinetics measured separately with a single-wavelength 400 nm probe fit using the same function.

centered at 775 nm. Kinetic traces taken from both the GSB (Fig. 6B) and the ESA (Fig. 6C) are fit well by a single exponential term convolved with a Gaussian instrument response function (IRF) with an average time constant of 3.8 ns with no evidence of a long-lived component. Again, we may conclude that ground state recovery from the ^{3}MC manifold is 3.8 ns.

Near-infrared excitation. To determine whether ground state recovery occurs directly from the $^3T_1$ band or instead from the $^3T_2$ band, we also performed fs-resolved OTA measurements using near-infrared (NIR; 800 nm) excitation to pump the $^3T_2$ band directly. The spectra shown in Fig. 7A appear essentially identical to those in Figs. 5 and 6, but the kinetic traces taken at the peaks of both the GSB in Fig. 7B and the ESA in Fig. 7C do not show the 9 ps rise characteristic of the ESA following excitation at 500 or 560 nm. Instead, both traces may be fit with only an ultrafast rise and a slow decay, with average time constants of 1.0 ps and a 2.6 ns; fitting the traces with two few-ps components reduces the norm of the residuals by <1%. The difference between the visible- and NIR-excitation early time kinetics is highlighted in Fig. S5. Taken together, these results demonstrate that the OTA spectrum observed beyond the first several ps at any excitation energy below the LMCT band corresponds to the lowest energy $^3T_2$ state rather than any of the $^3T_1$ states. Furthermore, while intraband relaxation within the $^3T_1$ manifold occurs faster than 300 fs, IC to the $^3T_2$ manifold occurs with a relatively sluggish lifetime of 9 ps. The 1.2 ps lifetimes found in the visible- and NIR-excitation kinetics are then attributable to a combination of vibrational relaxation and solvent reorganization. Importantly, we note that the 9 ps lifetime for the $^3T_1 \rightarrow {}^3T_2$ IC manifests as a rise in the ESA only and not the GSB, while the components associated with vibrational relaxation and ground state recovery appear in both the ESA and GSB as expected.

Ultraviolet excitation. Broadband ultrafast OTA spectra following excitation at 267 nm are shown in Fig. 8A. A broad, featureless ESA spans the entire probe spectrum for all Δt > 0. A representative kinetic trace taken at a probe wavelength of 590 nm is plotted in Fig. 8B (black dots) with a fit (red line) to the sum of three exponential decays and a step function, all convolved with a Gaussian IRF (see Fig. S6A for the individual fit components). The same fit was performed across the full probe spectrum to give the decay-associated spectra (DAS) shown in Fig. S6B. Importantly, there is very little variation in the time constant of each component between 550 and 700 nm as shown in Fig. S6C, demonstrating that our fitting model is indeed representative of the full dataset. Each component is positive in sign at all probe wavelengths, meaning each corresponds to decay of ESA rather than GSB or stimulated emission. Additionally, any contributions to the OTA kinetics from hydrated electrons generated by two-photon ionization of the solvent are negligible after the first 0.5 ps (see Figs. S8-S9 and accompanying discussion in SI). The time constants obtained by averaging over the DAS are 0.4 ± 0.2 ps, 10 ± 4 ps, and 300 ± 200 ps, with approximately 25% of the initial signal persisting beyond the 1 ns measurement window.

Perhaps surprisingly, the spectra in Fig. 8A do not closely resemble those in Figs. 5A and 5D. But because the XTA data shows that ~90% of the excited state fraction relaxes to the ^{3}MC manifold within 100 ps, we must then conclude that the OTA signal within the spectral window of our white light probe is substantially greater in magnitude for the LMCT states than for the $^3T_2$. This may be confirmed by comparing the ns OTA spectra averaged over different temporal windows shown in Fig. 9A. The spectrum averaged between 12 and 200 ns following UV excitation (blue) corresponds exclusively to the ^{5}LMCT state as the $^3T_2$ state has a lifetime of 3.8 ns, and this spectrum indeed resembles those in Fig. 8A. As expected, the spectrum averaged over the same window following visible excitation (yellow) shows no signal whatsoever, while the same spectrum averaged over the first two $^3T_2$ lifetimes (red) resembles those in Figs. 5A and 5D. It is also likely, however, that some difference between the

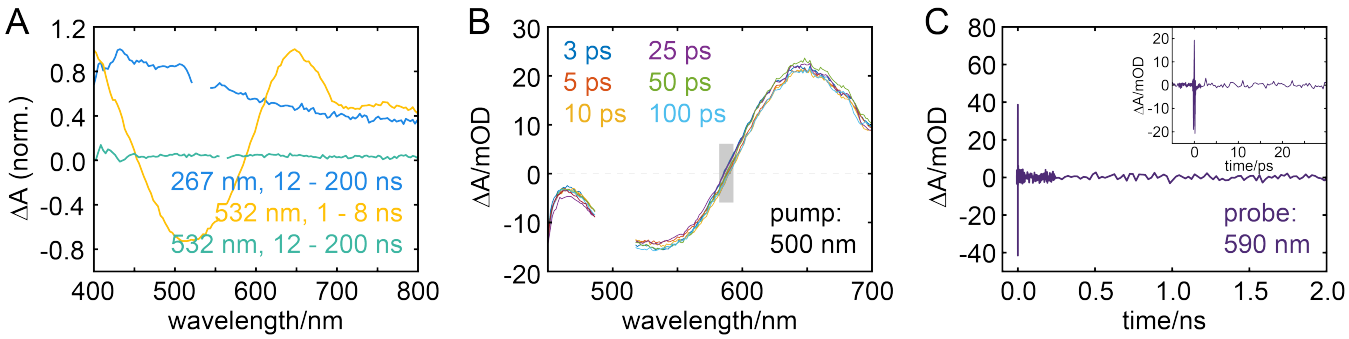

Figure 9. Separating ISC and IC kinetics. (A) OTA spectra averaged over short and long ns time windows. The spectrum averaged over 12-200 ns following UV excitation (blue) corresponds to the ^{5}LMCT state only, while the spectrum averaged over 1-8 ns following visible excitation (yellow) corresponds to the $^3T_2$ state only. The 12-200 ns spectrum following visible excitation (green) shows no TA signal. (B) Ultrafast OTA spectra following excitation at 500 nm at various $\Delta t > 0$, showing a consistent zero crossing at 590 nm. (C) Kinetic trace averaged over the spectral window centered at 590 nm indicated in panel (B) by the gray box. The first 30 ps are shown in the inset to highlight the lack of TA signal at all times after the coherent artifact.

shapes of the ultrafast OTA spectra obtained using visible and UV excitation arises from incomplete overlap of the more tightly focused UV pump beam with the spatially chirped white light continuum probe.

We are nevertheless faced with the challenge of separating the contributions from the ^{3}MC and ^{5}LMCT states if we wish to obtain lifetimes for the competing relaxation processes from the ^{3}LMCT state. One solution is evident from Fig. 9A-B, the latter of which shows ultrafast OTA spectra at several values of Δt following visible excitation: the ^{3}MC OTA spectrum has a zero crossing at 590 nm that is nearly invariant for all $\Delta t > 0$. The kinetic trace obtained by averaging across the spectral window in Fig. 9B indicated by the gray box is plotted in Fig. 9C, and indeed, only a sub-ps coherent artifact is apparent. Accordingly, any dynamics measured at 590 nm cannot contain contributions from relaxation *from* or *within* the ^{3}MC states. Because we expect little difference between the OTA spectra of the triplet and quintet LMCT states in the vicinity of the *d-d* band, any decay in the OTA signal at 590 nm must then correspond to either relaxation from the ^{3}LMCT state *into* the ^{3}MC manifold or formation of chemically distinct Fe(V) species, *i.e.*, photochemical products. Approaching the near-UV where LMCT transitions dominate the spectrum, however, we expect the magnitude of the ^{5}LMCT ESA to be lower than that of the ^{3}LMCT state due to the smaller number of spin-allowed LMCT transitions. Decay in this region thus reflects all relaxation processes from the ^{3}LMCT state.

The two intermediate components from the fit of the kinetic trace at 590 nm in Fig. 8B have time constants of 8 ± 3 ps and 210 ± 130 ps (95% confidence intervals). If we assume one of these corresponds to relaxation into the ^{3}MC manifold, we predict the corresponding ISC time constants to be 72 ± 27 ps and 2000 ± 1200 ps, respectively, using the 9:1 branching ratio estimated from the XTA data. Meanwhile, the two intermediate components from the fit of the kinetic trace at 400 nm in Fig. 8C (measured using the second harmonic of the laser as a single-wavelength probe) are 5 ± 6 and 45 ± 24 ps. The first of these is consistent with the 8 ± 3 ps component observed at 590 nm, and the second is consistent with the corresponding 72 ± 27 ps time constant predicted for ISC; no evidence of a ~2 ns component is observed at any probe wavelength. Together, these observations support the model in which IC from the ^{3}LMCT state into the ^{3}MC manifold occurs with a lifetime of 8 ps and ISC with a lifetime of 45 ps, giving a 15% quantum yield for ISC. This value is in good agreement with the 10% quantum yield estimated from the XTA data; however, because that analysis required us to make assumptions regarding the relative magnitudes of difference features, we expect the quantum yield obtained from the branching ratio measured by OTA to be more accurate. The 8 ps IC lifetime is also comparable to the 9 ps $^3T_1 \rightarrow {}^3T_2$ IC lifetime obtained from the visible-excitation data, lending more support for this assignment. A likely assignment for the 210 ± 130 ps decay observed across the white light probe spectrum but not at 400 nm, then, is the formation of $[FeO_3OH]^{2-}$, the dominant protonation state of aqueous ferrate(V) at pH 8.6.[9] The *d-d* band of aqueous $[FeO_3OH]^-$ is dramatically attenuated relative to that of $[FeO_4]^{2-}$ while the absorption at 400 nm is nearly identical for the two species,[40] and it is reasonable to expect similar behavior for ferrate(V). The lifetime is also consistent with those commonly measured for photoinduced proton-coupled electron transfer from water[79] and other protic solvents[80] to organic dyes.

Although these assignments are fully consistent with the entire body of OTA and XTA data presented here, we nevertheless cannot rule out a model in which both relaxation processes from the ^{3}LMCT state occur on the sub-ps timescale. The widths (FWHM) of the Gaussian IRFs measured for the white light continuum and 400 nm probe experiments are 0.26 ± 0.05 ps and 0.17 ± 0.05 ps, respectively, and it is possible that this temporal resolution is simply insufficient to identify multiple distinct fs decay components. In that case, the 8 ps, 45 ps, and 210 ps time constants would then all presumably correspond to downstream reactions of the long-lived ferrate(V) species ($[FeO_4]^{3-}$) following ISC. The spin state sensitivity afforded by Kβ X-ray emission spectroscopy[81] with the >50 ps

temporal resolution of a storage ring source[82,83] could provide a sufficient test of the slower model, though emission measurements with fs resolution (*i.e.*, using a hard X-ray free electron laser) would likely be necessary to reach a definitive conclusion.

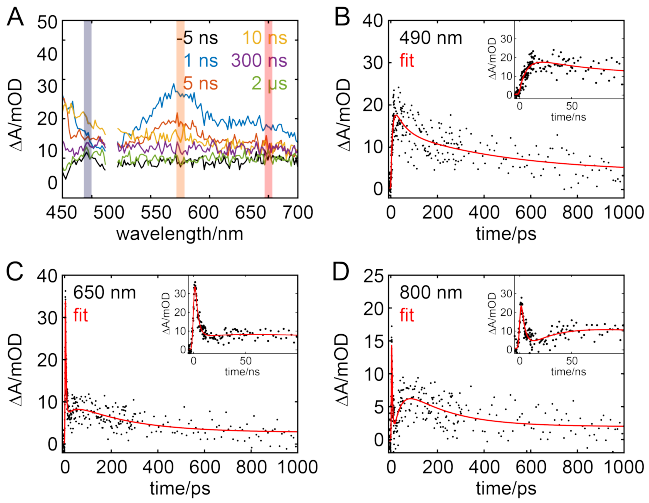

Figure 10. Nanosecond OTA spectra and kinetics with UV excitation. (A) OTA spectra plotted at several values of Δt following excitation at 267 nm, showing features consistent with both the $^3T_2$ and ^{5}LMCT states. (B) Kinetic trace averaged over the spectral window centered at 490 nm indicated in panel (A) by the gray vertical bar. The data points (black dots) are fit (red curve) to the sum of three exponential terms and a step function, all convolved with a Gaussian IRF. The inset shows the rise of the trace at Δt < 100 ns. (C) Kinetic trace of the ESA averaged over the spectral window centered at 650 nm indicated in panel (A) by the peach vertical bar fit using the same function. (C) Kinetic trace of the ESA averaged over the spectral window centered at 800 nm indicated in panel (A) by the salmon vertical bar fit using the same function.

Finally, we consider the fate(s) of the species contributing to the signal beyond the first several ns by analyzing the ns OTA experiments using 267 nm excitation. The OTA spectra in Fig. 10A show the distinct GSB and ESA peaks of the $^3T_2$ state that decay with the anticipated 3.8 ns time constant, after which the spectrum only shows the broad, featureless ESA of the ^{5}LMCT state. As expected, the sign of the 3.8 ns decay component obtained from multiexponential fits is negative at 490 nm (Fig. 10B) and positive at 650 and 800 nm (Fig. 10C-D). The DAS (Fig. S7) show two additional time constants of ~35 and ~300 ns at all probe wavelengths as well as a substantial population that persists beyond the 10 µs measurement window, in excellent agreement with the high repetition rate XTA results shown in Figs. 3 and S2. Importantly, the ~300 ns component accounts for <20% of the total OTA signal across nearly the entire probe bandwidth. Thus, while the low repetition rate XTA results shown in Fig. 4 demonstrate that the majority of the ~300 ns decay observed by high repetition rate XTA arises from sample refreshment, the OTA results demonstrate that some metastable and/or excited state dynamics indeed occur on a commensurate timescale. Notably, the signs of the longer components in the OTA data are reversed relative to those from the XTA data – that is, the 35 ns component is negative while the 300 ns component is positive. This observation will likely provide important clues regarding the origin of these components, but such analysis is beyond the scope of the current work. For now, we hypothesize they correspond to diffusion-limited reactions of $[FeO_3OH]^{2-}$, including coordination of water ligands to give an octahedral complex[40] and/or formation of a diferrate species,[84] though we do not have direct evidence to support this. Although these longer time constants are consistent with the XTA measurements, which selectively probe the iron, we have also performed a series of control experiments to confirm that our OTA measurements using UV excitation do not contain contributions from hydrated electrons generated by two-photon ionization of the aqueous environment. The details of these experiments and the corresponding data analysis are presented in Section 3 of the SI, and the results clearly demonstrate that the longer

Table 2. Time constants obtained from OTA kinetic fits with 95% confidence intervals.

Pump (nm)	**267**			**500**		**560**		**800**	
Probe (nm)	400	590		530	650	530	650	530	650
τ_1 **(ps)**	0.6 ± 0.4	0.3 ± 0.1		1.7 ± 0.3	0.5 ± 0.3	1.6 ± 0.4	1.2 ± 0.9	1.4 ± 1.0	0.6 ± 0.2
τ_2 **(ps)**	5 ± 6	8 ± 3		x	8 ± 7	x	10 ± 9	x	x
τ_3 **(ps)**	45 ± 24	210 ± 130		x	x	x	x	x	x
τ_4 **(ns)**	>> 3	>> 3		3.8 ± 0.3	3.3 ± 0.2	3.6 ± 0.4	3.5 ± 0.3	2.6 ± 0.5	2.6 ± 0.3
Probe (nm)	490	650	800			490	650		
τ_4 **(ns)**	7.3 ± 5.2	2.8 ± 0.8	3.9 ± 2.1			3.9 ± 0.8	3.7 ± 0.4		
τ_5 **(ns)**	43 ± 65	36 ± 66	30 ± 25			x	x		
τ_6 **(ns)**	470 ± 200	250 ± 140	200 ± 120			x	x		
τ_7 **(µs)**	>> 10	>> 10	>> 10			x	x		

An entry of 'x' means no component was observed; an empty entry means the measurement was not performed.

time constants may indeed be attributed to the ferrate(V) intermediate species rather than hydrated electrons.

Overall relaxation mechanism

The results discussed above may be summarized compactly in the Jablonski diagram shown in Fig. 11. We note that wherever possible, the lifetimes shown here were calculated by averaging those obtained from all relevant discrete probe measurements or averaging those obtained from the DAS across the region(s) of the broadband probe(s) for which significant OTA signal was observed (this process is described in detail in the SI). As a result, while some of the average lifetimes shown in the diagram vary from those reported in Table 2 for individual probe wavelengths, these lifetimes always fall within the 95% confidence intervals given in the table.

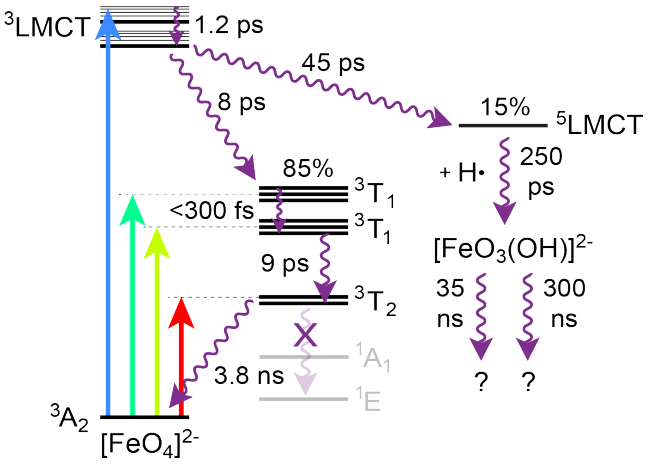

Figure 11. Jablonski diagram for aqueous ferrate(VI) at room temperature. The competing photophysical (left) and photochemical (right) relaxation pathways (purple curvy arrows) following UV excitation (straight blue arrow) are shown with the lifetimes of the individual steps. The energy levels corresponding to the visible and NIR excitation wavelengths used in this work are also indicated with straight arrows (aquamarine, 500 nm; yellow-green, 560 nm; red, 800 nm).

We propose that the initially populated ^{3}LMCT branches between a photophysical path in which it relaxes to the ground state *via* IC to the ^{3}MC states and a photochemical path in which it converts irreversibly to an Fe(V) species following ISC to the ^{5}LMCT state. Because IC occurs much more rapidly than ISC (8 ps vs. 45 ps), the photophysical path accounts for ~85% of the relaxation. We also find that ground state recovery occurs with a lifetime of 3.8 ns. Because the OTA spectra at Δt > 10 ps are identical in shape regardless of whether the sample is pumped using visible or NIR radiation, we conclude that ground state recovery occurs from the lowest energy $^3T_2$ state rather than from the lowest energy $^3T_1$ state; this is also consistent with the lack of visible or near-infrared emission at room temperature in solution following UV or visible excitation. While both the $^3T_1 \rightarrow {}^3A_2$ and $^3T_2 \rightarrow {}^3A_2$ transitions are spin-allowed, the latter is symmetry forbidden and thus expected to have a longer radiative lifetime as well as a faster nonradiative lifetime in accordance with the energy gap law. Thus, while fluorescence could be expected from the $^3T_1$ state if it persisted beyond a few ps, the 3.8 ns IC process is able to outcompete emission from the $^3T_2$ state.

Notably, the fs OTA kinetics following excitation at 500 or 560 nm in Figs. 5 and S4 show a clear non-impulsive growth within the first few ps that is entirely absent from the kinetics following excitation at 267 or 800 nm. The 9 ps time constant of the exponential growth term is visibly distinct from both the 500 fs decay term found in the UV-excitation kinetics and the 300 fs coherent artifact, and thus we assign this term to the $^3T_1 \rightarrow {}^3T_2$ transition. Because IC from the ^{3}LMCT state occurs in 8 ps and the subsequent 9 ps IC between ^{3}T states results in a change in ESA of opposite sign (*i.e.*, a growth), the subsequent 9 ps transition is not observed in the UV-excitation kinetics; on the other hand, intraband relaxation within the $^3T_2$ manifold occurs on the sub-ps timescale, and thus the subsequent 9 ps transition may be clearly seen. Like those observed in the visible- and NIR-excitation kinetics, the 500 fs term in the UV-excitation kinetics is likely attributable to a combination of vibrational relaxation and solvent reorganization, but because the distinctively polyphasic coherent artifact observed in the visible- and NIR-excitation kinetics (Fig. S4) is not present, it is unclear what the magnitude and duration of the nonresonant solvent response is. Accordingly, the 500 fs lifetime is taken to be only a qualitative estimate of the vibrational relaxation and solvent reorganization processes following UV-excitation.

The photochemical path is directly related to UV activation of ferrate(VI) for water treatment, as it yields the more highly oxidizing Fe(V) (and ultimately Fe(IV)) species. Following ISC, we believe that abstraction of a hydrogen atom from a solvent molecule (either in a single step as a true hydrogen atom transfer or through sequential proton and electron transfer steps) occurs in 210 ps to give [FeO$_3$OH]$^{2-}$ which then undergoes subsequent intermolecular reactions with lifetimes of 35 and 300 ns to give metastable species that persist beyond several tens of μs. This agrees with the ms lifetimes of ferrate(V) species measured using pulse radiolysis.[35,40,41] Time-resolved EXAFS measurements would help confirm these assignments and identify the long-lived and metastable species, though such experiments would be especially challenging due to the instability of ferrate(VI) under X-ray irradiation and the lack of commercial sources of bulk quantities of potassium ferrate(VI).

Importantly, we performed all experiments at a pH of 8.6, at which the protonation equilibria of ferrate(VI) and ferrate(V) give almost exclusively [FeO$_4$]$^{2-}$ and [FeO$_3$OH]$^{2-}$, respectively. Although this pH was initially chosen simply to slow the spontaneous reduction of aqueous ferrate(VI) at room temperature, it also dramatically simplifies the analysis of the transient absorption data. In our model, we make the assumptions that only the dominant (unprotonated) ferrate(VI) species exists prior to excitation and only the dominant (monoprotonated) ferrate(V) species is formed directly from the ^{5}LMCT state.

Intersystem crossing and internal conversion rates

The 45 ps lifetime assigned to ISC is substantially longer than the well-known sub-200 fs ISC lifetime between the MLCT and MC states in $[Fe(2,2'\text{-bipyridine})_3]^{2+}$.[85] However, ISC lifetimes on the order of tens of ps are not uncommon among 3*d* transition metal complexes, including other d^2 species,[86] Fe(III) and Mn(III) porphyrins,[87,88] and tetrahedral Cu(I) dyes.[89–92] There are even some examples of 3*d* complexes exhibiting ISC lifetimes between charge transfer states on the order of tens of ns.[93] Furthermore, the lack of near-infrared emission from the ^1E state of ferrate(VI) at room temperature tells us that the lifetime for the $^3T_2 \rightarrow {}^1E$ ISC process must be substantially longer than the 3.8 ns lifetime for the $^3T_2 \rightarrow {}^3A_2$ IC process, similar to that typically observed between the low-lying MC states in Fe(II) thermal spin-crossover complexes.[94–99]

One reason for the slow ISC in ferrate(VI) may be the lack of structural distortion expected between the ground and excited states, which would result in nested potential energy surfaces and high energetic barriers for crossings between states; this may also account for the sluggishness of the spin-allowed $^3T_2 \rightarrow {}^3A_2$ IC.[75] The small number of vibrational degrees of freedom in this small complex also presumably results in sparse spin-vibrational/spin-vibronic manifolds of states that in other cases are directly responsible for facilitating rapid ISC.[100–102] Finally, the zero-field splittings in crystalline potassium ferrate(VI) measured by electron paramagnetic resonance are less than 0.07 cm^{-1},[103] demonstrating very weak spin-orbit coupling in the ground $^3A_2$ state that may also be true for the excited states.[2] The strong covalency in ferrate(VI) also likely results in substantial ligand-based character of the LMCT states, thereby limiting the impact of the heavy atom effect.[104] Confirming the long ISC lifetime and identifying its physical origin will require extensive computational work to calculate the potential energy surfaces of and spin-orbit coupling constants between the LMCT states, and we are currently working toward this goal.

Significance to water treatment applications

This work provides strong evidence of a metastable Fe(V) species, confirming prior deductions based on indirect techniques using probe compounds and spin traps. The role of Fe(V) in the (photo)activated ferrate system holds several points of relevance to the water treatment field. First, we can calculate a quantum yield for the formation of Fe(V), an essential step towards utilization of an AOP. Based on the analysis of the XTA and OTA data presented above, we estimate the quantum yield for formation of the metastable ferrate(V) species following UV excitation to be 15%. Although this is substantially lower than the ~50% quantum yield for the UV photolysis of H_2O_2 in aqueous solution (or equivalently, a 100% quantum yield for the formation of hydroxyl radicals),[105] the UV/ferrate(VI) combination has been shown to outperform UV/H_2O_2 for remediation of 2,4-dichlorophenol.[33] This is because the effective quantum yield for UV/H_2O_2 (~10%[19]) is much lower than the quantum yield of the photolysis itself: very high concentrations of H_2O_2 are required for water treatment with UV/H_2O_2 due to the extraordinarily low molar absorptivity of H_2O_2 at practical excitation wavelengths (*e.g.*, 23 $M^{-1}\cdot cm^{-1}$ at 250 nm[106]), but the excess H_2O_2 present also rapidly scavenges the hydroxyl radicals as they are formed.[107] Thus, the efficiency for photoinduced generation of metastable highly oxidizing species for these two systems is indeed quite comparable. Similar quantum yields of ~10% for hydroxyl radical formation from UV/O_3 have also been reported.[108] Although ozone shows much stronger UV absorption than H_2O_2, it must be constantly produced *in situ*, adding another degree of complexity to the water treatment process. Potassium ferrate(VI), on the other hand, shows similarly high UV absorption (>5000 cm^{-1} at 250 nm) and may be produced off-site and stored indefinitely under ambient conditions. The quantification of Fe(V) yield and identification of the relaxation mechanisms might help enable water treatment system optimization toward full scale adaptation.

These results also point to additional options for photoactivation of Fe(VI). The LMCT absorption band of ferrate(VI) likely extends well into the visible spectrum before parasitic absorption by the unproductive ligand field transitions begins to dominate,[74] allowing more energy-efficient blue and near-UV light to be used for activation. Using longer wavelength light would also greatly improve the photon economy for the photoactivated treatment of turbid water, as Rayleigh scattering of the incident light by suspended particulates scales dramatically as $1/\lambda^4$. This is especially valuable in a surface water context, where particle loads can vary widely.[109] The potential to form radical-like iron intermediates with longer wavelength light may prove an especially versatile and advantageous AOP, given the current paradigm of UV light dependence. We are currently working to measure the quantum yield for photoactivation of aqueous ferrate(VI) as a function of wavelength across this region to assess this possibility.

CONCLUSIONS

Ferrate(VI) is remarkably simple in structure and equally rich in excited state dynamics. And yet despite the broad range of potential applications for photoactivated aqueous ferrate(VI), those dynamics have remained mostly unexplored. A major reason for this is undoubtedly the challenges to spectroscopic analysis presented by a weakly absorbing species that spontaneously decomposes into insoluble particulates.

By combining the element specificity of XTA with the ultrafast temporal resolution of OTA, we have been able to overcome these limitations and map out the relaxation pathways of ferrate(VI) on timescales ranging from ~1 ps to hundreds of ns. The strong pre-edge feature in the Fe K-edge X-ray absorption spectrum provides an excellent probe of the 3*d* orbital occupation, which in turn allows us to differentiate between LMCT and MC states. We have found that the initially populated ^{3}LMCT states branches between IC into the ^{3}MC manifold and ISC into the ^{5}LMCT manifold on the timescale of tens of ps with a

quantum yield of ~15% for ISC. We believe the thermalized ^{5}LMCT state then reacts with water on the timescale of 100s of ps to yield the $[FeO_3OH]^{2-}$ species believed to be involved in the oxidation of recalcitrant TOCs, though direct evidence is necessary to confirm this assignment. We have also measured two additional time constants (35 ns and 300 ns) that may correspond to diffusion-limited reactions of $[FeO_3OH]^{2-}$, although these assignments remain unclear.

Photoactivation of ferrate(VI) to produce radical-like iron intermediates (*e.g.*, Fe(V)) may play an important role in a new generation of AOPs for water treatment, offering alternative approaches for tackling the pressing issue of TOCs. It offers several advantages over existing technologies, including shelf-stable inputs and non-toxic byproducts. The detailed picture of the competing photochemical and photophysical relaxation pathways of the LMCT state(s) of ferrate(VI) presented here will provide crucial information for comprehensive techno-economic assessments of AOPs employing the combination of ferrate(VI) and blue/UV light and prove essential to the development, optimization, and full-scale adoption of such technologies. Results here may also provide insight into the roles of Fe(V) and Fe(IV) formed in parallel work on chemical activation of ferrate with common reductants.

ASSOCIATED CONTENT

Supporting Information. General, XTA, and OTA experimental methods; kinetic, linear combination, and decay-associated analysis methods; and consideration of hydrated electrons and laser fluence. This material is available free of charge via the Internet at http://pubs.acs.org.

AUTHOR INFORMATION

Corresponding Author

* Dugan Hayes, Department of Chemistry, University of Rhode Island, Kingston, Rhode Island 02881, United States. Email: dugan@uri.edu

Notes

The authors declare no competing financial interest.

ACKNOWLEDGMENT

This material is based upon work supported by the U.S. Department of Energy, Office of Science, Office of Basic Energy Sciences, under Award DE-SC0019429, which supported all work by C.A., B.T.Y., and D.H. All work by J.E.G. and C.D.S. was supported by the U.S. National Science Foundation, Division of Chemical Bioengineering, Environmental, and Transport Systems (CBET) under CAREER Award 2046383. G.D, A.M.M and C.O. were supported by the US Department of Energy, Office of Science, Office of Basic Energy Sciences, Chemical Sciences, Geosciences and Biosciences Division under award # DE-AC02-06CH11357. This research used resources of the Advanced Photon Source, a U.S. Department of Energy (DOE) Office of Science User Facility operated for the DOE Office of Science by Argonne National Laboratory under Contract No. DE-AC02-06CH11357. All XTA data were collected at beamlines 7-ID-D and 11-ID-D at the Advanced Photon Source, Argonne National Laboratory. The authors acknowledge and thank Element 26 Technology (400 Hobbs Road, Suite 107, League City, TX 77546; soundar.ramchandran@gmail.com; jtstrehl@gmail.com) for supplying the potassium ferrate(VI) product used in this study.

ABBREVIATIONS

XTA, X-ray transient absorption; OTA, optical transient absorption; XANES, X-ray absorption near-edge structure; IRF, instrument response function; DAS, decay-associated spectrum; UV, ultraviolet; NIR, near-infrared; LMCT, ligand-to-metal charge transfer; MC, metal-centered; IC, internal conversion; ISC, intersystem crossing; GSB, ground state bleach; ESA, excited state absorption; TOC, trace organic contaminant; AOP, advanced oxidation process.

REFERENCES

(1) Engineering, N. A. of; National Academies of Sciences, Engineering, and Medicine. *Environmental Engineering for the 21st Century: Addressing Grand Challenges*; The National Academies Press: Washington, DC, 2019. https://doi.org/10.17226/25121.

(2) Schmidbaur, H. The History and the Current Revival of the Oxo Chemistry of Iron in Its Highest Oxidation States: Fe^{VI} – Fe^{VIII}. *Z. Anorg. Allgem. Chem.* **2018**, *644* (12–13), 536–559. https://doi.org/10.1002/zaac.201800036.

(3) Audette, R. J.; Quail, J. W.; Smith, P. J. Ferrate (VI) Ion, a Novel Oxidizing Agent. *Tetrahedron Lett.* **1971**, *12* (3), 279–282. https://doi.org/10.1016/S0040-4039(01)96418-4.

(4) Johnson, M. D.; Hornstein, B. J. Unexpected Selectivity in the Oxidation of Arylamines with Ferrate–Preliminary Mechanistic Considerations. *Chem. Commun.* **1996**, No. 8, 965–966. https://doi.org/10.1039/CC9960000965.

(5) Delaude, L.; Laszlo, P. A Novel Oxidizing Reagent Based on Potassium Ferrate(VI). *J. Org. Chem.* **1996**, *61* (18), 6360–6370. https://doi.org/10.1021/jo960633p.

(6) Ho, C.-M.; Lau, T.-C. Lewis Acid Activated Oxidation of Alkanes by Barium Ferrate. *New J. Chem.* **2000**, *24* (8), 587–590. https://doi.org/10.1039/B002907F.

(7) Zhou, Y.; Zhang, Z.-Y.; Huang, X.; Li, J.; Li, T. Versatile Functionalization of Carbon Nanomaterials by Ferrate(VI). *Nanomicro Lett.* **2020**, *12* (1), 32. https://doi.org/10.1007/s40820-019-0353-2.

(8) Sharma, V. K.; Chen, L.; Zboril, R. Review on High Valent Fe^{VI} (Ferrate): A Sustainable Green Oxidant in Organic Chemistry and Transformation of Pharmaceuticals. *ACS Sustainable Chem. Eng.* **2016**, *4* (1), 18–34. https://doi.org/10.1021/acssuschemeng.5b01202.

(9) Sharma, V. K. Ferrate(VI) and Ferrate(V) Oxidation of Organic Compounds: Kinetics and Mechanism. *Coord. Chem. Rev.* **2013**, *257* (2), 495–510. https://doi.org/10.1016/j.ccr.2012.04.014.

(10) Sharma, V. K.; Zboril, R.; Varma, R. S. Ferrates: Greener Oxidants with Multimodal Action in Water Treatment Technologies. *Acc. Chem. Res.* **2015**, *48* (2), 182–191. https://doi.org/10.1021/ar5004219.

(11) Dar, A. A.; Pan, B.; Qin, J.; Zhu, Q.; Lichtfouse, E.; Usman, M.; Wang, C. Sustainable Ferrate Oxidation: Reaction Chemistry, Mechanisms and Removal of Pollutants in Wastewater. *Environ. Pollut.* **2021**, *290*, 117957. https://doi.org/10.1016/j.envpol.2021.117957.

(12) Thompson, G. W.; Ockerman, L. T.; Schreyer, J. M. Preparation and Purification of Potassium Ferrate. VI. *J. Am. Chem. Soc.* **1951**, *73* (3), 1379–1381. https://doi.org/10.1021/ja01147a536.

(13) Williams, D. H.; Riley, J. T. Preparation and Alcohol Oxidation Studies of the Ferrate(VI) Ion, FeO_4^{2-}. *Inorg. Chim. Acta* **1974**, *8*, 177–183. https://doi.org/10.1016/S0020-1693(00)92612-4.

(14) Bouzek, K.; Roušar, I. Current Efficiency during Anodic Dissolution of Iron to Ferrate(VI) in Concentrated Alkali Hydroxide Solutions. *J. Appl. Electrochem.* **1993**, *23* (12), 1317–1322. https://doi.org/10.1007/BF00234818.

(15) Monzyk, B. F.; Rose, J. K.; Burckle, E. C.; Clark, T. O.; Smeltz, A. D.; Rider, D. G. Electrochemical Method and Apparatus for Producing Ferrate(VI), August 4, 2005.

(16) Mácová, Z.; Bouzek, K.; Híveš, J.; Sharma, V. K.; Terryn, R. J.; Baum, J. C. Research Progress in the Electrochemical Synthesis of Ferrate(VI). *Electrochim. Acta* **2009**, *54* (10), 2673–2683. https://doi.org/10.1016/j.electacta.2008.11.034.

(17) Lim, M.-H.; Snyder, S. A.; Sedlak, D. L. Use of Biodegradable Dissolved Organic Carbon (BDOC) to Assess the Potential for Transformation of Wastewater-Derived Contaminants in Surface Waters. *Water Res.* **2008**, *42* (12), 2943–2952. https://doi.org/10.1016/j.watres.2008.03.008.

(18) Aslani, H.; Nasseri, S.; Nabizadeh, R.; Mesdaghinia, A.; Alimohammadi, M.; Nazmara, S. Haloacetic Acids Degradation by an Efficient Ferrate/UV Process: Byproduct Analysis, Kinetic Study, and Application of Response Surface Methodology for Modeling and Optimization. *J. Environ. Manage.* **2017**, *203*, 218–228. https://doi.org/10.1016/j.jenvman.2017.07.072.

(19) Miklos, D. B.; Remy, C.; Jekel, M.; Linden, K. G.; Drewes, J. E.; Hübner, U. Evaluation of Advanced Oxidation Processes for Water and Wastewater Treatment – A Critical Review. *Water Res.* **2018**, *139*, 118–131. https://doi.org/10.1016/j.watres.2018.03.042.

(20) Gilca, A. F.; Teodosiu, C.; Fiore, S.; Musteret, C. P. Emerging Disinfection Byproducts: A Review on Their Occurrence and Control in Drinking Water Treatment Processes. *Chemosphere* **2020**, *259*, 127476. https://doi.org/10.1016/j.chemosphere.2020.127476.

(21) Oturan, M. A.; Aaron, J.-J. Advanced Oxidation Processes in Water/Wastewater Treatment: Principles and Applications. A Review. *Crit. Rev. Env. Sci. Technol.* **2014**, *44* (23), 2577–2641. https://doi.org/10.1080/10643389.2013.829765.

(22) Jiang, J.-Q.; Lloyd, B. Progress in the Development and Use of Ferrate(VI) Salt as an Oxidant and Coagulant for Water and Wastewater Treatment. *Water Res.* **2002**, *36* (6), 1397–1408. https://doi.org/10.1016/S0043-1354(01)00358-X.

(23) DeLuca, S. J.; Chao, A. C.; Smallwood, C. Ames Test of Ferrate Treated Water. *J. Environ. Eng.* **1983**, *109* (5), 1159–1167. https://doi.org/10.1061/(ASCE)0733-9372(1983)109:5(1159).

(24) Goodwill, J. E.; Jiang, Y.; Reckhow, D. A.; Gikonyo, J.; Tobiason, J. E. Characterization of Particles from Ferrate Preoxidation. *Environ. Sci. Technol.* **2015**, *49* (8), 4955–4962. https://doi.org/10.1021/acs.est.5b00225.

(25) Feng, M.; Jinadatha, C.; McDonald, T. J.; Sharma, V. K. Accelerated Oxidation of Organic Contaminants by Ferrate(VI): The Overlooked Role of Reducing Additives. *Environ. Sci. Technol.* **2018**, *52* (19), 11319–11327. https://doi.org/10.1021/acs.est.8b03770.

(26) Shao, B.; Dong, H.; Sun, B.; Guan, X. Role of Ferrate(IV) and Ferrate(V) in Activating Ferrate(VI) by Calcium Sulfite for Enhanced Oxidation of Organic Contaminants. *Environ. Sci. Technol.* **2019**, *53* (2), 894–902. https://doi.org/10.1021/acs.est.8b04990.

(27) Gao, Y.; Zhou, Y.; Pang, S.-Y.; Wang, Z.; Shen, Y.-M.; Jiang, J. Quantitative Evaluation of Relative Contribution of High-Valent Iron Species and Sulfate Radical in Fe(VI) Enhanced Oxidation Processes via Sulfur Reducing Agents Activation. *Chem. Eng. J.* **2020**, *387*, 124077. https://doi.org/10.1016/j.cej.2020.124077.

(28) Manoli, K.; Nakhla, G.; Ray, A. K.; Sharma, V. K. Oxidation of Caffeine by Acid-Activated Ferrate(VI): Effect of Ions and Natural Organic Matter. *AIChE J.* **2017**, *63* (11), 4998–5006. https://doi.org/10.1002/aic.15878.

(29) Ghosh, M.; Manoli, K.; Renaud, J. B.; Sabourin, L.; Nakhla, G.; Sharma, V. K.; Ray, A. K. Rapid Removal of Acesulfame Potassium by Acid-Activated Ferrate(VI) under Mild Alkaline Conditions. *Chemosphere* **2019**, *230*, 416–423. https://doi.org/10.1016/j.chemosphere.2019.05.069.

(30) Sun, S.; Jiang, J.; Qiu, L.; Pang, S.; Li, J.; Liu, C.; Wang, L.; Xue, M.; Ma, J. Activation of Ferrate by Carbon Nanotube for Enhanced Degradation of Bromophenols: Kinetics, Products, and Involvement of Fe(V)/Fe(IV). *Water Res.* **2019**, *156*, 1–8. https://doi.org/10.1016/j.watres.2019.02.057.

(31) Pan, B.; Feng, M.; McDonald, T. J.; Manoli, K.; Wang, C.; Huang, C.-H.; Sharma, V. K. Enhanced Ferrate(VI) Oxidation of Micropollutants in Water by Carbonaceous Materials: Elucidating Surface Functionality. *Chem. Eng. J.* **2020**, *398*, 125607. https://doi.org/10.1016/j.cej.2020.125607.

(32) Yang, T.; Mai, J.; Cheng, H.; Zhu, M.; Wu, S.; Tang, L.; Liang, P.; Jia, J.; Ma, J. UVA-LED-Assisted Activation of the Ferrate(VI) Process for Enhanced Micropollutant Degradation: Important Role of Ferrate(IV) and Ferrate(V). *Environ. Sci. Technol.* **2022**, *56* (2), 1221–1232. https://doi.org/10.1021/acs.est.1c03725.

(33) Wu, S.; Liu, H.; Lin, Y.; Yang, C.; Lou, W.; Sun, J.; Du, C.; Zhang, D.; Nie, L.; Yin, K.; Zhong, Y. Insights into Mechanisms of UV/Ferrate Oxidation for Degradation of Phenolic Pollutants: Role of Superoxide Radicals. *Chemosphere* **2020**, *244*, 125490. https://doi.org/10.1016/j.chemosphere.2019.125490.

(34) Sharma, V. K. Oxidation of Inorganic Contaminants by Ferrates (VI, V, and IV)–Kinetics and Mechanisms: A Review. *J. Environ. Manage.* **2011**, *92* (4), 1051–1073. https://doi.org/10.1016/j.jenvman.2010.11.026.

(35) Sharma, V. K. Ferrate(V) Oxidation of Pollutants: A Premix Pulse Radiolysis Study. *Radiat. Phys. Chem.* **2002**, *65* (4), 349–355. https://doi.org/10.1016/S0969-806X(02)00335-3.

(36) Bielski, B. H. J.; Sharma, V. K.; Czapski, G. Reactivity of Ferrate(V) with Carboxylic Acids: A Pre-Mix Pulse Radiolysis Study. *Radiat. Phys. Chem.* **1994**, *44* (5), 479–484. https://doi.org/10.1016/0969-806X(94)90044-2.

(37) Feng, M.; Sharma, V. K. Enhanced Oxidation of Antibiotics by Ferrate(VI)-Sulfur(IV) System: Elucidating Multi-Oxidant Mechanism. *Chem. Eng. J.* **2018**, *341*, 137–145. https://doi.org/10.1016/j.cej.2018.01.112.

(38) Sun, S.; Pang, S.; Jiang, J.; Ma, J.; Huang, Z.; Zhang, J.; Liu, Y.; Xu, C.; Liu, Q.; Yuan, Y. The Combination of Ferrate(VI) and Sulfite as a Novel Advanced Oxidation Process for Enhanced Degradation of Organic Contaminants. *Chem. Eng. J.* **2018**, *333*, 11–19. https://doi.org/10.1016/j.cej.2017.09.082.

(39) Bielski, B. H. J.; Thomas, M. J. Studies of Hypervalent Iron in Aqueous Solutions. 1. Radiation-Induced Reduction of Iron(VI) to Iron(V) by CO_2^-. *J. Am. Chem. Soc.* **1987**, *109* (25), 7761–7764. https://doi.org/10.1021/ja00259a026.

(40) Rush, J. D.; Bielski, B. H. J. Kinetics of Ferrate(V) Decay in Aqueous Solution. A Pulse-Radiolysis Study. *Inorg. Chem.* **1989**, *28* (21), 3947–3951. https://doi.org/10.1021/ic00320a004.

(41) Rush, J. D.; Bielski, B. H. J. Decay of Ferrate(V) in Neutral and Acidic Solutions. A Premix Pulse Radiolysis Study. *Inorg. Chem.* **1994**, *33* (24), 5499–5502. https://doi.org/10.1021/ic00102a024.

(42) Sharma, V. K.; Rivera, W.; Joshi, V. N.; Millero, F. J.; O'Connor, D. Ferrate(VI) Oxidation of Thiourea. *Environ. Sci. Technol.* **1999**, *33* (15), 2645–2650. https://doi.org/10.1021/es981083a.

(43) Sarma, R.; Angeles-Boza, A. M.; Brinkley, D. W.; Roth, J. P. Studies of the Di-Iron(VI) Intermediate in Ferrate-

Dependent Oxygen Evolution from Water. *J. Am. Chem. Soc.* **2012**, *134* (37), 15371–15386. https://doi.org/10.1021/ja304786s.

(44) Novak, P.; Kolar, M.; Machala, L.; Siskova, K. M.; Karlicky, F.; Petr, M.; Zboril, R. Transformations of Ferrates(IV,V,VI) in Liquids: Mössbauer Spectroscopy of Frozen Solutions. *Phys. Chem. Chem. Phys.* **2018**, *20* (48), 30247–30256. https://doi.org/10.1039/C8CP05952G.

(45) Harischandra, D. N.; Zhang, R.; Newcomb, M. Photochemical Generation of a Highly Reactive Iron–Oxo Intermediate. A True Iron(V)–Oxo Species? *J. Am. Chem. Soc.* **2005**, *127* (40), 13776–13777. https://doi.org/10.1021/ja0542439.

(46) Torres-Alacan, J.; Lindner, J.; Vöhringer, P. Probing the Primary Photochemical Processes of Octahedral Iron(V) Formation with Femtosecond Mid-Infrared Spectroscopy. *ChemPhysChem* **2015**, *16* (11), 2289–2293. https://doi.org/10.1002/cphc.201500370.

(47) Pan, Z.; Zhang, R.; Fung, L. W.-M.; Newcomb, M. Photochemical Production of a Highly Reactive Porphyrin–Iron–Oxo Species. *Inorg. Chem.* **2007**, *46* (5), 1517–1519. https://doi.org/10.1021/ic061972w.

(48) Rohde, J.-U.; Torelli, S.; Shan, X.; Lim, M. H.; Klinker, E. J.; Kaizer, J.; Chen, K.; Nam, W.; Que, L. Structural Insights into Nonheme Alkylperoxoiron(III) and Oxoiron(IV) Intermediates by X-Ray Absorption Spectroscopy. *J. Am. Chem. Soc.* **2004**, *126* (51), 16750–16761. https://doi.org/10.1021/ja047667w.

(49) Aliaga-Alcalde, N.; George, S. D.; Mienert, B.; Bill, E.; Wieghardt, K.; Neese, F. The Geometric and Electronic Structure of $[(Cyclam\text{-}Acetato)Fe(N)]^{+}$: A Genuine Iron(V) Species with a Ground-State Spin $S=1/2$. *Angew. Chem. Int. Ed.* **2005**, *44* (19), 2908–2912. https://doi.org/10.1002/anie.200462368.

(50) Bukowski, M. R.; Koehntop, K. D.; Stubna, A.; Bominaar, E. L.; Halfen, J. A.; Münck, E.; Nam, W.; Que, L. A Thiolate-Ligated Nonheme Oxoiron(IV) Complex Relevant to Cytochrome P450. *Science* **2005**, *310* (5750), 1000–1002. https://doi.org/10.1126/science.1119092.

(51) Klinker, E. J.; Jackson, T. A.; Jensen, M. P.; Stubna, A.; Juhász, G.; Bominaar, E. L.; Münck, E.; Que, L. A Tosylimido Analogue of a Nonheme Oxoiron(IV) Complex. *Angew. Chem. Int. Ed.* **2006**, *45* (44), 7394–7397. https://doi.org/10.1002/anie.200602799.

(52) Rohde, J.-U.; Stubna, A.; Bominaar, E. L.; Münck, E.; Nam, W.; Que, L. Nonheme Oxoiron(IV) Complexes of Tris(2-Pyridylmethyl)Amine with Cis-Monoanionic Ligands. *Inorg. Chem.* **2006**, *45* (16), 6435–6445. https://doi.org/10.1021/ic060740u.

(53) Berry, J. F.; Bill, E.; Bothe, E.; George, S. D.; Mienert, B.; Neese, F.; Wieghardt, K. An Octahedral Coordination Complex of Iron(VI). *Science* **2006**, *312* (5782), 1937–1941. https://doi.org/10.1126/science.1128506.

(54) Rohde, J.-U.; Betley, T. A.; Jackson, T. A.; Saouma, C. T.; Peters, J. C.; Que, L. XAS Characterization of a Nitridoiron(IV) Complex with a Very Short Fe–N Bond. *Inorg. Chem.* **2007**, *46* (14), 5720–5726. https://doi.org/10.1021/ic700818q.

(55) de Oliveira, F. T.; Chanda, A.; Banerjee, D.; Shan, X.; Mondal, S.; Que, L.; Bominaar, E. L.; Munck, E.; Collins, T. J. Chemical and Spectroscopic Evidence for an Fe^{V}-Oxo Complex. *Science* **2007**, *315* (5813), 835–838. https://doi.org/10.1126/science.1133417.

(56) Jackson, T. A.; Rohde, J.-U.; Seo, M. S.; Sastri, C. V.; DeHont, R.; Stubna, A.; Ohta, T.; Kitagawa, T.; Münck, E.; Nam, W.; Que, L. Axial Ligand Effects on the Geometric and Electronic Structures of Nonheme Oxoiron(IV) Complexes. *J. Am. Chem. Soc.* **2008**, *130* (37), 12394–12407. https://doi.org/10.1021/ja8022576.

(57) England, J.; Martinho, M.; Farquhar, E. R.; Frisch, J. R.; Bominaar, E. L.; Münck, E.; Que, L. A Synthetic High-Spin Oxoiron(IV) Complex: Generation, Spectroscopic Characterization, and Reactivity. *Angew. Chem. Int. Ed.* **2009**, *48* (20), 3622–3626. https://doi.org/10.1002/anie.200900863.

(58) Chandrasekaran, P.; Stieber, S. C. E.; Collins, T. J.; Lawrence Que, J.; Neese, F.; DeBeer, S. Prediction of High-Valent Iron K-Edge Absorption Spectra by Time-Dependent Density Functional Theory. *Dalton Trans.* **2011**, *40* (42), 11070–11079. https://doi.org/10.1039/C1DT11331C.

(59) Bigi, J. P.; Harman, W. H.; Lassalle-Kaiser, B.; Robles, D. M.; Stich, T. A.; Yano, J.; Britt, R. D.; Chang, C. J. A High-Spin Iron(IV)–Oxo Complex Supported by a Trigonal Nonheme Pyrrolide Platform. *J. Am. Chem. Soc.* **2012**, *134* (3), 1536–1542. https://doi.org/10.1021/ja207048h.

(60) Hong, S.; Sutherlin, K. D.; Vardhaman, A. K.; Yan, J. J.; Park, S.; Lee, Y.-M.; Jang, S.; Lu, X.; Ohta, T.; Ogura, T.; Solomon, E. I.; Nam, W. A Mononuclear Nonheme Iron(V)-Imido Complex. *J. Am. Chem. Soc.* **2017**, *139* (26), 8800–8803. https://doi.org/10.1021/jacs.7b04695.

(61) Sabenya, G.; Lázaro, L.; Gamba, I.; Martin-Diaconescu, V.; Andris, E.; Weyhermüller, T.; Neese, F.; Roithova, J.; Bill, E.; Lloret-Fillol, J.; Costas, M. Generation, Spectroscopic, and Chemical Characterization of an Octahedral Iron(V)-Nitrido Species with a Neutral Ligand Platform. *J. Am. Chem. Soc.* **2017**, *139* (27), 9168–9177. https://doi.org/10.1021/jacs.7b00429.

(62) Hunter, B. M.; Thompson, N. B.; Müller, A. M.; Rossman, G. R.; Hill, M. G.; Winkler, J. R.; Gray, H. B. Trapping an Iron(VI) Water-Splitting Intermediate in Nonaqueous Media. *Joule* **2018**, *2* (4), 747–763. https://doi.org/10.1016/j.joule.2018.01.008.

(63) Dantignana, V.; Serrano-Plana, J.; Draksharapu, A.; Magallón, C.; Banerjee, S.; Fan, R.; Gamba, I.; Guo, Y.; Que, L.; Costas, M.; Company, A. Spectroscopic and Reactivity Comparisons between Nonheme Oxoiron(IV) and Oxoiron(V) Species Bearing the Same Ancillary Ligand. *J. Am. Chem. Soc.* **2019**, *141* (38), 15078–15091. https://doi.org/10.1021/jacs.9b05758.

(64) Sabenya, G.; Gamba, I.; Gómez, L.; Clémancey, M.; Frisch, J. R.; Klinker, E. J.; Blondin, G.; Torelli, S.; Que, L.; Martin-Diaconescu, V.; Latour, J.-M.; Lloret-Fillol, J.; Costas, M. Octahedral Iron(IV)–Tosylimido Complexes Exhibiting Single Electron-Oxidation Reactivity. *Chem. Sci.* **2019**, *10* (41), 9513–9529. https://doi.org/10.1039/C9SC02526J.

(65) Ezhov, R.; Ravari, A. K.; Pushkar, Y. Characterization of the Fe^{V}=O Complex in the Pathway of Water Oxidation. *Angew. Chem. Int. Ed.* **2020**, *132* (32), 13604–13607. https://doi.org/10.1002/ange.202003278.

(66) Martinez, J. L.; Lutz, S. A.; Yang, H.; Xie, J.; Telser, J.; Hoffman, B. M.; Carta, V.; Pink, M.; Losovyj, Y.; Smith, J. M. Structural and Spectroscopic Characterization of an Fe(VI) Bis(Imido) Complex. *Science* **2020**.

(67) Oswald, V. F.; Lee, J. L.; Biswas, S.; Weitz, A. C.; Mittra, K.; Fan, R.; Li, J.; Zhao, J.; Hu, M. Y.; Alp, E. E.; Bominaar, E. L.; Guo, Y.; Green, M. T.; Hendrich, M. P.; Borovik, A. S. Effects of Noncovalent Interactions on High-Spin Fe(IV)–Oxido Complexes. *J. Am. Chem. Soc.* **2020**, *142* (27), 11804–11817. https://doi.org/10.1021/jacs.0c03085.

(68) Tanabe, Y.; Sugano, S. On the Absorption Spectra of Complex Ions II. *J. Phys. Soc. Jpn.* **1954**, *9* (5), 766–779. https://doi.org/10.1143/JPSJ.9.766.

(69) Carrington, A.; Schonland, D.; Symons, M. C. R. Structure and Reactivity of the Oxyanions of Transition Metals. Part IV. Some Relations between Electronic Spectra and Structure. *J. Chem. Soc.* **1957**, No. 0, 659–665. https://doi.org/10.1039/JR9570000659.

(70) Orgel, L. E. The Visible Spectrum of the Hypomanganate Ion. *Mol. Phys.* **1964**, *7* (4), 397–399. https://doi.org/10.1080/00268976300101161.

(71) Itoh, Y. Single-Crystal Electronic Absorption Spectra of $MMnO_4$ (M=K, Rb, Cs), K_2CrO_4, K_2MnO_4, and K_2FeO_4. *J. Spectrosc. Soc. Japan* **1976**, *25* (2), 83–93. https://doi.org/10.5111/bunkou.25.83.

(72) Herren, M.; Güdel, H. U. Ferrate(VI), a Novel near-Infrared Luminophore. *Inorg. Chem.* **1992**, *31* (18), 3683–3684. https://doi.org/10.1021/ic00044a001.

(73) Brunold, T. C.; Hauser, A.; Güdel, H. U. Absorption and Luminescence Spectroscopy of Ferrate (VI) Doped into Crystals of K_2MO_4 (M = S, Se, Cr, Mo). *J. Lumin.* **1994**, *59* (5), 321–332. https://doi.org/10.1016/0022-2313(94)90059-0.

(74) Al-Abdalla, A.; Seijo, L.; Barandiarán, Z. A New Interpretation of the Bonding and Spectroscopy of the Tetraoxoferrate(VI) FeO_4^{2-} Ion. *J. Chem. Phys.* **1998**, *109* (15), 6396–6405. https://doi.org/10.1063/1.477283.

(75) Brunold, T. C.; Güdel, H. U.; Kück, S.; Huber, G. Excited State Properties of Ferrate(VI) Doped Crystals of K_2SO_4 and K_2CrO_4. *J. Lumin.* **1996**, *65*, 293–301. https://doi.org/10.1016/0022-2313(95)00082-8.

(76) Farmand, M.; Licht, S.; Ramaker, D. Studying the Reversibility of Multielectron Charge Transfer in Fe(VI) Cathodes Utilizing X-Ray Absorption Spectroscopy. *J. Phys. Chem. C* **2013**, *117* (39), 19875–19884. https://doi.org/10.1021/jp406626x.

(77) March, A. M.; Doumy, G.; Andersen, A.; Al Haddad, A.; Kumagai, Y.; Tu, M.-F.; Bang, J.; Bostedt, C.; Uhlig, J.; Nascimento, D. R.; Assefa, T. A.; Németh, Z.; Vankó, G.; Gawelda, W.; Govind, N.; Young, L. Elucidation of the Photoaquation Reaction Mechanism in Ferrous Hexacyanide Using Synchrotron X-Rays with Sub-Pulse-Duration Sensitivity. *J. Chem. Phys.* **2019**, *151* (14), 144306. https://doi.org/10.1063/1.5117318.

(78) Westre, T. E.; Kennepohl, P.; DeWitt, J. G.; Hedman, B.; Hodgson, K. O.; Solomon, E. I. A Multiplet Analysis of Fe K-Edge 1s → 3d Pre-Edge Features of Iron Complexes. *J. Am. Chem. Soc.* **1997**, *119* (27), 6297–6314. https://doi.org/10.1021/ja964352a.

(79) Rabe, E. J.; Corp, K. L.; Sobolewski, A. L.; Domcke, W.; Schlenker, C. W. Proton-Coupled Electron Transfer from Water to a Model Heptazine-Based Molecular Photocatalyst. *J. Phys. Chem. Lett.* **2018**, *9* (21), 6257–6261. https://doi.org/10.1021/acs.jpclett.8b02519.

(80) Jonely, M.; Noriega, R. Role of Polar Protic Solvents in the Dissociation and Reactivity of Photogenerated Radical Ion Pairs. *J. Phys. Chem. B* **2020**, *124* (15), 3083–3089. https://doi.org/10.1021/acs.jpcb.9b11299.

(81) Lafuerza, S.; Carlantuono, A.; Retegan, M.; Glatzel, P. Chemical Sensitivity of Kβ and Kα X-Ray Emission from a Systematic Investigation of Iron Compounds. *Inorg. Chem.* **2020**, *59* (17), 12518–12535. https://doi.org/10.1021/acs.inorgchem.0c01620.

(82) Haldrup, K.; Vankó, G.; Gawelda, W.; Galler, A.; Doumy, G.; March, A. M.; Kanter, E. P.; Bordage, A.; Dohn, A.; van Driel, T. B.; Kjær, K. S.; Lemke, H. T.; Canton, S. E.; Uhlig, J.; Sundström, V.; Young, L.; Southworth, S. H.; Nielsen, M. M.; Bressler, C. Guest–Host Interactions Investigated by Time-Resolved X-Ray Spectroscopies and Scattering at MHz Rates: Solvation Dynamics and Photoinduced Spin Transition in Aqueous $Fe(Bipy)_3^{2+}$. *J. Phys. Chem. A* **2012**, *116* (40), 9878–9887. https://doi.org/10.1021/jp306917x.

(83) Britz, A.; Gawelda, W.; Assefa, T. A.; Jamula, L. L.; Yarranton, J. T.; Galler, A.; Khakhulin, D.; Diez, M.; Harder, M.; Doumy, G.; March, A. M.; Bajnóczi, É.; Németh, Z.; Pápai, M.; Rozsályi, E.; Sárosiné Szemes, D.; Cho, H.; Mukherjee, S.; Liu, C.; Kim, T. K.; Schoenlein, R. W.; Southworth, S. H.; Young, L.; Jakubikova, E.; Huse, N.; Vankó, G.; Bressler, C.; McCusker, J. K. Using Ultrafast X-Ray Spectroscopy To Address Questions in Ligand-Field Theory: The Excited State Spin and Structure of $[Fe(Dcpp)_2]^{2+}$. *Inorg. Chem.* **2019**, *58* (14), 9341–9350. https://doi.org/10.1021/acs.inorgchem.9b01063.

(84) Chen, G.; Lam, W. W. Y.; Lo, P.-K.; Man, W.-L.; Chen, L.; Lau, K.-C.; Lau, T.-C. Mechanism of Water Oxidation by Ferrate(VI) at pH 7–9. *Chem. Eur. J.* **2018**, *24* (70), 18735–18742. https://doi.org/10.1002/chem.201803757.

(85) Monat, J. E.; McCusker, J. K. Femtosecond Excited-State Dynamics of an Iron(II) Polypyridyl Solar Cell Sensitizer Model. *J. Am. Chem. Soc.* **2000**, *122* (17), 4092–4097. https://doi.org/10.1021/ja9924360.

(86) Dorn, M.; Kalmbach, J.; Boden, P.; Päpcke, A.; Gómez, S.; Förster, C.; Kuczelinis, F.; Carrella, L. M.; Büldt, L. A.; Bings, N. H.; Rentschler, E.; Lochbrunner, S.; González, L.; Gerhards, M.; Seitz, M.; Heinze, K. A Vanadium(III) Complex with Blue and NIR-II Spin-Flip Luminescence in Solution. *J. Am. Chem. Soc.* **2020**, *142* (17), 7947–7955. https://doi.org/10.1021/jacs.0c02122.

(87) Gonçalves, P. J.; De Boni, L.; Borissevitch, I. E.; Zílio, S. C. Excited State Dynamics of Meso-Tetra(Sulphonatophenyl) Metalloporphyrins. *J. Phys. Chem. A* **2008**, *112* (29), 6522–6526. https://doi.org/10.1021/jp800589j.

(88) Jung, J.; Ohkubo, K.; Goldberg, D. P.; Fukuzumi, S. Photocatalytic Oxygenation of 10-Methyl-9,10-Dihydroacridine by O_2 with Manganese Porphyrins. *J. Phys. Chem. A* **2014**, *118* (32), 6223–6229. https://doi.org/10.1021/jp505860f.

(89) Siddique, Z. A.; Yamamoto, Y.; Ohno, T.; Nozaki, K. Structure-Dependent Photophysical Properties of Singlet and Triplet Metal-to-Ligand Charge Transfer States in Copper(I) Bis(Diimine) Compounds. *Inorg. Chem.* **2003**, *42* (20), 6366–6378. https://doi.org/10.1021/ic034412v.

(90) Shaw, G. B.; Grant, C. D.; Shirota, H.; Castner, E. W.; Meyer, G. J.; Chen, L. X. Ultrafast Structural Rearrangements in the MLCT Excited State for Copper(I) Bis-Phenanthrolines in Solution. *J. Am. Chem. Soc.* **2007**, *129* (7), 2147–2160. https://doi.org/10.1021/ja067271f.

(91) Iwamura, M.; Takeuchi, S.; Tahara, T. Real-Time Observation of the Photoinduced Structural Change of Bis(2,9-Dimethyl-1,10-Phenanthroline)Copper(I) by Femtosecond Fluorescence Spectroscopy: A Realistic Potential Curve of the Jahn–Teller Distortion. *J. Am. Chem. Soc.* **2007**, *129* (16), 5248–5256. https://doi.org/10.1021/ja069300s.

(92) Bergmann, L.; Hedley, G. J.; Baumann, T.; Bräse, S.; Samuel, I. D. W. Direct Observation of Intersystem Crossing in a Thermally Activated Delayed Fluorescence Copper Complex in the Solid State. *Sci. Adv.* **2016**, *2* (1), e1500889. https://doi.org/10.1126/sciadv.1500889.

(93) Föller, J.; Kleinschmidt, M.; Marian, C. M. Phosphorescence or Thermally Activated Delayed Fluorescence? Intersystem Crossing and Radiative Rate Constants of a Three-Coordinate Copper(I) Complex Determined by Quantum-Chemical Methods. *Inorg. Chem.* **2016**, *55* (15), 7508–7516. https://doi.org/10.1021/acs.inorgchem.6b00818.

(94) Beattie, J. K.; Sutin, Norman.; Turner, D. H.; Flynn, G. W. Rate of Intersystem Crossing between ^1A and ^5A States of an Iron(II) Complex in Solutions. *J. Am. Chem. Soc.* **1973**, *95* (6), 2052–2054. https://doi.org/10.1021/ja00787a078.

(95) Hoselton, M. A.; Drago, R. S.; Wilson, L. J.; Sutin, N. Direct Measurement of Spin-State Lifetimes in Solution for Some Iron(II) Spin Equilibrium Complexes Derived from Hexadentate Ligands. *J. Am. Chem. Soc.* **1976**, *98* (22), 6967–6969. https://doi.org/10.1021/ja00438a036.

(96) Beattie, J. K.; Binstead, R. A.; West, R. J. Intersystem Crossing Observed by Ultrasonic Relaxation of the Singlet-Quintet Spin Equilibrium of Iron(II) Complexes in Solution. *J. Am. Chem. Soc.* **1978**, *100* (10), 3044–3050. https://doi.org/10.1021/ja00478a016.

(97) Dose, E. V.; Hoselton, M. A.; Sutin, N.; Tweedle, M. F.; Wilson, L. J. Dynamics of Intersystem Crossing Processes in Solution for Six-Coordinate d^5, d^6, and d^7 Spin-Equilibrium Metal

Complexes of Iron(III), Iron(II), and Cobalt(II). *J. Am. Chem. Soc.* **1978**, *100* (4), 1141–1147. https://doi.org/10.1021/ja00472a017.

(98) Decurtins, S.; Gutlich, P.; Hasselbach, K. M.; Hauser, A.; Spiering, H. Light-Induced Excited-Spin-State Trapping in Iron(II) Spin-Crossover Systems. Optical Spectroscopic and Magnetic Susceptibility Study. *Inorg. Chem.* **1985**, *24* (14), 2174–2178. https://doi.org/10.1021/ic00208a013.

(99) Pandeya, K. B.; Singh, R.; Prakash, C.; Baijal, J. S. New Observations on a Tris(Dithiocarbamato)Iron(III) Complex: Magnetic and Mössbauer Studies. *Inorg. Chem.* **1987**, *26* (19), 3216–3218. https://doi.org/10.1021/ic00266a030.

(100) Gawelda, W.; Cannizzo, A.; Pham, V.-T.; van Mourik, F.; Bressler, C.; Chergui, M. Ultrafast Nonadiabatic Dynamics of $[Fe^{II}(Bpy)_3]^{2+}$ in Solution. *J. Am. Chem. Soc.* **2007**, *129* (26), 8199–8206. https://doi.org/10.1021/ja070454x.

(101) Lemke, H. T.; Kjær, K. S.; Hartsock, R.; van Driel, T. B.; Chollet, M.; Glownia, J. M.; Song, S.; Zhu, D.; Pace, E.; Matar, S. F.; Nielsen, M. M.; Benfatto, M.; Gaffney, K. J.; Collet, E.; Cammarata, M. Coherent Structural Trapping through Wave Packet Dispersion during Photoinduced Spin State Switching. *Nat. Commun.* **2017**, *8* (1), 15342. https://doi.org/10.1038/ncomms15342.

(102) Penfold, T. J.; Gindensperger, E.; Daniel, C.; Marian, C. M. Spin-Vibronic Mechanism for Intersystem Crossing. *Chem. Rev.* **2018**, *118* (15), 6975–7025. https://doi.org/10.1021/acs.chemrev.7b00617.

(103) Carrington, A.; Ingram, D. J. E.; Lott, K. a. K.; Schonland, D. S.; Symons, M. C. R.; Pryce, M. H. L. Electron Resonance Studies of Transition Metal Oxyions, I. Experimental Results for the Manganate, Hypomanganate and Ferrate Ions. *Proc. R. Soc. London, Ser. A* **1960**, *254* (1276), 101–110. https://doi.org/10.1098/rspa.1960.0007.

(104) Hsu, C.-W.; Lin, C.-C.; Chung, M.-W.; Chi, Y.; Lee, G.-H.; Chou, P.-T.; Chang, C.-H.; Chen, P.-Y. Systematic Investigation of the Metal-Structure–Photophysics Relationship of Emissive d^{10}-Complexes of Group 11 Elements: The Prospect of Application in Organic Light Emitting Devices. *J. Am. Chem. Soc.* **2011**, *133* (31), 12085–12099. https://doi.org/10.1021/ja2026568.

(105) Goldstein, S.; Aschengrau, D.; Diamant, Y.; Rabani, J. Photolysis of Aqueous H_2O_2: Quantum Yield and Applications for Polychromatic UV Actinometry in Photoreactors. *Environ. Sci. Technol.* **2007**, *41* (21), 7486–7490. https://doi.org/10.1021/es071379t.

(106) Morgan, M. S.; Van Trieste, P. F.; Garlick, S. M.; Mahon, M. J.; Smith, A. L. Ultraviolet Molar Absorptivities of Aqueous Hydrogen Peroxide and Hydroperoxyl Ion. *Anal. Chim. Acta* **1988**, *215*, 325–329. https://doi.org/10.1016/S0003-2670(00)85294-0.

(107) Parsons, S. *Advanced Oxidation Processes for Water and Wastewater Treatment*; IWA Publishing, 2004.

(108) Reisz, E.; Schmidt, W.; Schuchmann, H.-P.; von Sonntag, C. Photolysis of Ozone in Aqueous Solutions in the Presence of Tertiary Butanol. *Environ. Sci. Technol.* **2003**, *37* (9), 1941–1948. https://doi.org/10.1021/es0113100.

(109) Ouyang, Y.; Nkedi-Kizza, P.; Wu, Q. T.; Shinde, D.; Huang, C. H. Assessment of Seasonal Variations in Surface Water Quality. *Water Res.* **2006**, *40* (20), 3800–3810. https://doi.org/10.1016/j.watres.2006.08.030.

For Table of Contents Only